

2

AD-A277 226



NAVAL POSTGRADUATE SCHOOL Monterey, California



S DTIC
ELECTE
MAR 25 1994
E D

THESIS

FINITE ELEMENT ANALYSIS OF DAMAGE IN
FIBROUS COMPOSITES USING A
MICROMECHANICAL MODEL

by

Joseph Michael Berner

December, 1993

Thesis Advisor: Young W. Kwon

Approved for public release; distribution is unlimited.

85P1

94-09099



94 3 22 017

REPORT DOCUMENTATION PAGE			Form Approved OMB No. 0704	
Public reporting burden for this collection of information is estimated to average 1 hour per response, including the time for reviewing instruction, searching existing data sources, gathering and maintaining the data needed, and completing and reviewing the collection of information. Send comments regarding this burden estimate or any other aspect of this collection of information, including suggestions for reducing this burden, to Washington headquarters Services, Directorate for Information Operations and Reports, 1215 Jefferson Davis Highway, Suite 1204, Arlington, VA 22202-4302, and to the Office of Management and Budget, Paperwork Reduction Project (0704-0188) Washington DC 20503.				
1. AGENCY USE ONLY		2. REPORT DATE December 1993	3. REPORT TYPE AND DATES COVERED Engineer's Thesis	
4. TITLE AND SUBTITLE FINITE ELEMENT ANALYSIS OF DAMAGE IN FIBROUS COMPOSITES USING A MICROMECHANICAL MODEL			5. FUNDING NUMBERS	
6. AUTHOR(S) <i>Joseph Michael Berner</i>				
7. PERFORMING ORGANIZATION NAME(S) AND ADDRESS(ES) Naval Postgraduate School Monterey, CA 93943-5000			8. PERFORMING ORGANIZATION REPORT NUMBER	
9. SPONSORING/MONITORING AGENCY NAME(S) AND ADDRESS(ES)			10. SPONSORING/MONITORING AGENCY REPORT NUMBER	
11. SUPPLEMENTARY NOTES The views expressed in this thesis are those of the author and do not reflect the official policy or position of the Department of Defense or the U.S. Government.				
12a. DISTRIBUTION/AVAILABILITY STATEMENT Approved for public release; distribution is unlimited.			12b. DISTRIBUTION CODE *A	
13. ABSTRACT The objective of this investigation is to study the damage mechanics of composite structures using a micromechanical approach for determining strength and stiffness degradation of the composite structures as damages, such as matrix cracking and fiber breakage, progress. The micromechanical cell method provides for analysis of stress at the fiber and matrix level while providing smeared composite properties for global structural analysis. As a result, the damage and failure criteria are expressed in terms of the fiber and matrix stress level of the composite structure. A correlation for stiffness reduction due to transverse cracking of a ceramic matrix composite under tensile loading is implemented in a three-dimensional finite element model. Next, thermal residual stresses from fabrication of the ceramic matrix composite are incorporated into the analysis. Finally, the finite element method is applied to a polymer matrix composite laminate with a center hole in order to study the progression of damage and final failure during tensile loading. The comparisons between the present predictions and the experimental results for the previous examples are very good.				
14. SUBJECT TERMS FIBROUS COMPOSITE, DAMAGE MECHANICS, FAILURE CRITERIA, STIFFNESS REDUCTION, MICROMECHANICS, FINITE ELEMENT METHOD			15. NUMBER OF PAGES 85	
			16. PRICE CODE	
17. SECURITY CLASSIFICATION OF REPORT Unclassified XX	18. SECURITY CLASSIFICATION OF THIS PAGE Unclassified	19. SECURITY CLASSIFICATION OF ABSTRACT Unclassified	20. LIMITATION OF ABSTRACT Unclassified	

Approved for public release; distribution is unlimited.

**Finite Element Analysis of Damage in Fibrous Composites
Using A Micromechanical Model**

by

**Joseph M. Berner
Commander, United States Navy
B.S., United States Naval Academy, Annapolis, MD**

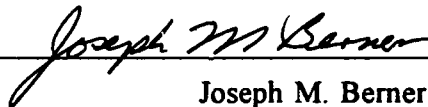
Submitted in partial fulfillment
of the requirements for the degrees of

**MASTER OF SCIENCE IN MECHANICAL ENGINEERING
and
MECHANICAL ENGINEER**

from the

**NAVAL POSTGRADUATE SCHOOL
December 1993**

Author:



Joseph M. Berner

Approved by:



Young W. Kwon, Thesis Advisor



Matthew D. Kelleher, Chairman

Department of Mechanical Engineering



Richard S. Elster, Dean of Instruction

ABSTRACT

The objective of this investigation is to study the damage mechanics of composite structures using a micromechanical approach for determining strength and stiffness degradation of the composite structures as damages, such as matrix cracking and fiber breakage, progress. The micromechanical cell method provides for analysis of stress at the fiber and matrix level while providing smeared composite properties for global structural analysis. As a result, the damage and failure criteria are expressed in terms of the fiber and matrix stress level of the composite structure. A correlation for stiffness reduction due to transverse cracking of a ceramic matrix composite under tensile loading is implemented in a three-dimensional finite element model. Next, thermal residual stresses from fabrication of the ceramic matrix composite are incorporated into the analysis. Finally, the finite element method is applied to a polymer matrix composite laminate with a center hole in order to study the progression of damage and final failure during tensile loading. The comparisons between the present predictions and the experimental results for the previous examples are very good.

Accession For	
NTIS CRA&I	<input checked="" type="checkbox"/>
DTIC TAB	<input type="checkbox"/>
Unannounced	<input type="checkbox"/>
Justification	
By	
Distribution /	
Availability Codes	
Dist	Avail and/or Special
A-1	

TABLE OF CONTENTS

I. INTRODUCTION	1
A. BACKGROUND	1
B. DETERMINING COMPOSITE MATERIAL PROPERTIES	2
C. THE MICROMECHANICAL CELL MODEL	5
II. FINITE ELEMENT MODEL DEVELOPMENT	10
A. ANALYTICAL DERIVATION	10
B. FORTRAN COMPUTER PROGRAM DEVELOPMENT	23
III. STIFFNESS REDUCTION OF A CERAMIC MATRIX COMPOSITE	26
A. OVERVIEW	26
B. EXPERIMENTAL BASIS	28
C. MATRIX STIFFNESS REDUCTION CORRELATION	29
D. FEM STIFFNESS REDUCTION RESULTS	31
E. PARAMETRIC STUDY	38
IV. STIFFNESS REDUCTION MODIFIED BY THERMAL RESIDUAL STRESS	40

A.	BACKGROUND	40
B.	DERIVATION	41
1.	Unidirectional Case	41
2.	Cross-Ply Case	42
C.	FEM STIFFNESS REDUCTION WITH THERMAL RESIDUAL STRESS	44
V.	DAMAGE PROGRESSION AND FAILURE IN A POLYMER MATRIX COMPOSITE	48
A.	OVERVIEW	48
B.	FAILURE CRITERIA AND MODELLING	49
C.	FEM DAMAGE PROGRESSION STUDY	51
VI.	SUMMARY AND CONCLUSIONS	63
A.	SUMMARY	63
B.	CONCLUSIONS	64
	LIST OF REFERENCES	66
	APPENDIX A - EQUATIONS FOR FEM DERIVATION	70

APPENDIX B - THERMAL STRESS DERIVATION USING KWON CELL

METHOD 72

INITIAL DISTRIBUTION LIST 7

I. INTRODUCTION

A. BACKGROUND

Modern structural designs increasingly incorporate man-made composite materials in applications that require components with special material properties which are unavailable from conventional metals or alloys. From the structural mechanics viewpoint, composites are typically used to improve either the stiffness-to-weight ratio or the strength-to-weight ratio of a structural member. Naval shipboard applications of composite materials are typically dependent on these weight savings when a composite material is used to fulfill a specified stiffness or strength requirement. Current naval composite applications include main propulsion shafting, decks, superstructures, small equipment foundations and graphite-reinforced-poly (GRP) auxiliary system piping. Although the composite material itself may actually cost more than its conventional metallic predecessor, incorporation of lightweight composite materials usually reduces total ship cost due to synergistic savings in the entire ship structure because of the reduced total ship weight.

Composite properties such as strength and stiffness are dependent upon the volume fraction of the fiber and the individual properties of the constituent fiber and matrix materials. The variation of the fiber volume fraction for a given composite allows the designer greater flexibility when incorporating composite materials into a structure. With this flexibility comes added complexity due to the fact that the optimum volume fraction

for a given stiffness may not be optimum for composite strength. And, composite material properties may vary due to damage accumulation such as matrix transverse cracking during the loading history of the composite member. This current research investigates the analysis of composite material properties, such as stiffness and strength, and their degradation using a three dimensional micromechanical model.

B. DETERMINING COMPOSITE MATERIAL PROPERTIES

The study of composite materials and structures can be undertaken from two different approaches: micromechanical and macromechanical. In the micromechanical approach, the properties of the constituent fiber and matrix materials and their interaction through stress-strain constitutive relations are analyzed in order to predict the overall behavior of the composite structural member. In the macromechanical approach, the properties of the constituent fiber and matrix materials are averaged or smeared to produce a set of pseudo-homogeneous properties for the composite structural member. The macromechanical approach has the advantage of requiring less detailed modeling in that individual fiber and matrix properties are only used initially in determining the smeared composite properties. Finite element models using the macromechanical approach are somewhat less complex and typically require less computational time than those models which are based on the micromechanical approach. However, the micromechanical approach provides more useful information such as the fiber and matrix stress and strain which are typically used for failure criteria or strength degradation computations. Thus, the more complex micromechanical approach is more useful when

analyzing damage mechanics and failure of composite material structures.

Under normal, non-damaging or elastic loading conditions, the stiffness properties of aligned, continuous, fiber composites can be predicted by the simple rule of mixtures (ROM). The ROM model uses the strength of materials approach and is based upon assumptions that the composite is loaded at low strain levels in the elastic region where no damage occurs in the fibers or matrix, that the fibers have uniform properties and are aligned parallel throughout the composite, that the matrix and fibers have a no-slip perfectly bonded interface, and that, for the longitudinally applied load case, there is equal strain in the fiber and matrix [Ref.1]. For composites which approximate these assumptions and which are loaded in the longitudinal direction along the fiber, ROM provides reasonable values for composite stiffness. However, for transverse loading with respect to the fiber axis, ROM does not accurately predict the composite stiffness.

Micromechanical models based on the theory of elasticity provide better overall results for aligned, parallel fiber composites [Ref. 2]. Noteworthy among the micromechanical models are the relations developed by C.C. Chamis [Ref. 3]: Chamis assumed that the matrix is isotropic and that the fibers are orthotropic. A composite with such constituents would have one plane of symmetry and therefore would be transversely isotropic. With the condition of transverse isotropy, Chamis reduced the problem from one with three dimensions to one with two dimensions. This method resulted in five independent properties in order to define a stress-strain constitutive relation for the smeared composite. Chamis and Sendekyj [Ref. 4] provide an excellent survey of the early micromechanics approach to predicting composite stiffness. Jones [Ref. 5]

succinctly presents methods for bounding stiffness properties of composites using variational energy approaches with classical elasticity theory and also describes the contiguity approach used to develop the famous Halpin-Tsai relations. These previous methods provide generally reasonable values for composite stiffness. But, these early micromechanical methods are often not sufficiently accurate or readily applied to structural computations involving composites. And, these methods are based on two-dimensional, linear elastic analysis while the real composite member is three dimensional, and typically behaves in nonlinear manner over its useful loading range [Ref. 6].

In recent years, there has been significant study of three-dimensional micromechanical models. Dvorak and Bahei-El-Din [Ref. 7] formulated an axisymmetric model for an elastic-plastic constitutive relation based on cylindrical fibers with surrounding matrix material. The axisymmetric assumption was considered physically valid and reduced the complexity of the three dimensional elasticity analysis for the micromechanical modelling of elastic-plastic deformation. Aboudi [Ref. 8] introduced the micromechanical method of cells based on the assumption that the composite material consisted of two repetitive phases of fiber and matrix materials. By assuming the repetitive or periodic nature of the fiber and matrix array, Aboudi was able to simplify his model by using a representative cell which consisted of four subcells. Although a view of his model appears to describe a square cell with one subcell of fiber and three subcells of matrix, the geometry of the fiber and matrix is not restricted due to calculation of the interface conditions on an average bases. Aboudi introduced the method of cells starting with simple unidirectional fiber composites and then extended his method to

discontinuous short fiber composites. Aboudi's micromechanical model is mathematically complex and computational intensive. Others, such as Pecknold [Ref. 9] noted that Aboudi's model forms the basis for a finite element model. Pecknold conducted an investigation of a simplified unit cell model. Kwon used a micromechanics model [Ref. 10, 11, 12] by focusing on the fiber and matrix stresses at the micromechanical level. Kwon later refined his original cell method [Ref. 6]. Kwon's micromechanics models are especially applicable for the investigation of composite damage because it considers both the fiber and matrix stress at the micromechanical level and thus allows specific fiber and matrix yield and/or failure criteria to be applied. The refined Kwon model [Ref. 6] formed the basis for this current work.

C. THE MICROMECHANICAL CELL MODEL

Similar to the Aboudi cell model, the Kwon model considers the composite as a unit cell composed of four subcells: one fiber subcell and three matrix subcells. The unit cell is represented by a three dimensional solid, the rectangular parallelepiped. Based on symmetry, only one-quarter of the total cell may be modeled as shown in Figure 1.1.

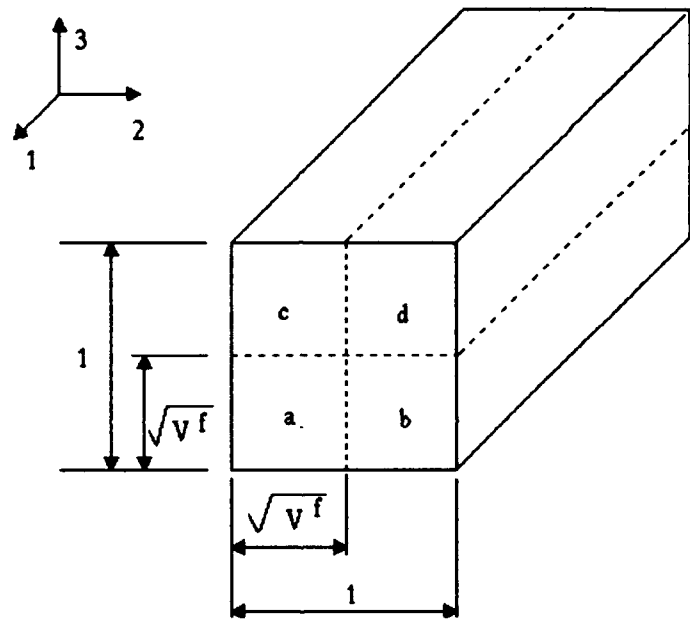


Figure 1.1 - The Kwon Micromechanical Model Unit Cell And Subcells

Note that the size of each cell is dependent on the fiber volume fraction. Kwon then expresses the composite stresses and strains as a function of the subcell stresses, the subcell strains, and the volume fraction as shown in Equations (1.1) and (1.2):

$$\bar{\sigma}_{ij} = V_f \sigma_{ij}^a + \sqrt{V_f} (1 - \sqrt{V_f}) \sigma_{ij}^b + \sqrt{V_f} (1 - \sqrt{V_f}) \sigma_{ij}^c + (1 - \sqrt{V_f})^2 \sigma_{ij}^d \quad i, j = 1, 3 \quad (1.1)$$

$$\bar{\epsilon}_{ij} = V_f \epsilon_{ij}^a + \sqrt{V_f} (1 - \sqrt{V_f}) \epsilon_{ij}^b + \sqrt{V_f} (1 - \sqrt{V_f}) \epsilon_{ij}^c + (1 - \sqrt{V_f})^2 \epsilon_{ij}^d \quad i, j = 1, 3 \quad (1.2)$$

where $\bar{\sigma}_{ij}$ and $\bar{\epsilon}_{ij}$ are composite stresses and strains, σ_{ij}^α and ϵ_{ij}^α are subcell ($\alpha = a, b, c,$ or d) stresses and strains, and V_f is the fiber volume fraction.

Note that subcell 'a' represents the fiber and subcells 'b', 'c', and 'd' represent the matrix. Thus, the composite smeared stress or strain values are equal to the volume average of the subcell stresses and strains. The condition of stress continuity is satisfied at the subcell interfaces as expressed by Equation (1.3).

$$\begin{aligned} \sigma_{22}^a &= \sigma_{22}^b, & \sigma_{22}^c &= \sigma_{22}^d, & \sigma_{33}^a &= \sigma_{33}^c, & \sigma_{33}^b &= \sigma_{33}^d \\ \sigma_{12}^a &= \sigma_{12}^b, & \sigma_{12}^c &= \sigma_{12}^d, & \sigma_{13}^a &= \sigma_{13}^c, & \sigma_{13}^b &= \sigma_{13}^d \\ \sigma_{23}^a &= \sigma_{23}^b, & \sigma_{23}^c &= \sigma_{23}^d, & \sigma_{23}^a &= \sigma_{23}^d \end{aligned} \quad (1.3)$$

Each subcell may have different strains, but the following strain compatibilities are assumed. The longitudinal strains of the subcells are equal and the sums of the transverse strains of the subcell in either transverse direction are also equal. The shearing strains must also satisfy similar conditions. Expressed mathematically, the strain conditions are shown in Equation (1.4).

$$\begin{aligned}
\varepsilon_{11}^a &= \varepsilon_{11}^b, & \varepsilon_{11}^a &= \varepsilon_{11}^c, & \varepsilon_{11}^a &= \varepsilon_{11}^d \\
\varepsilon_{22}^a + \varepsilon_{22}^b &= \varepsilon_{22}^c + \varepsilon_{22}^d, & \varepsilon_{33}^a + \varepsilon_{33}^c &= \varepsilon_{33}^b + \varepsilon_{33}^d \\
\varepsilon_{12}^a + \varepsilon_{12}^b &= \varepsilon_{12}^c + \varepsilon_{12}^d, & \varepsilon_{13}^a + \varepsilon_{13}^c &= \varepsilon_{13}^b + \varepsilon_{13}^d
\end{aligned} \tag{1.4}$$

The constitutive relation for each subcell is expressed by the generalized Hooke's law of Equation (1.5).

$$\sigma_{ij}^\alpha = E_{ijkl}^\alpha \varepsilon_{kl}^\alpha \quad i, j, k, l = 1, 2, 3 \text{ and } \alpha = a, b, c, d \tag{1.5}$$

Solving Equations (1.1) to (1.5) together yields the expression for smeared composite material properties in terms of fiber and matrix material properties and their volume fractions. In addition, the equations provide the following sequential relations: global displacements \rightarrow composite strains \rightarrow fiber and matrix strains \rightarrow fiber and matrix stresses \rightarrow composite stresses.

The global displacements are obtained from the finite element analyses of fibrous composite structures. For damage progression studies, the calculation of stress and strain at the fiber and matrix level allows failure criteria to be applied at that micro-level. Thus, numerical modeling using this method can provide insight into the micro-level failure process for composite materials.

For this current work, the Kwon micromechanical method of cells was implemented within the finite element program in order to perform several functions: First, the new micromechanical model was used to determine the smeared composite properties for use in computing the basic finite element stiffness matrix. Secondly, the model was implemented in the finite element post-processing routines to convert the finite element

displacement results into stresses and strains at the fiber and matrix micro-level. The fiber and matrix stress levels were used for either stiffness reduction or the application of failure criteria.

II. FINITE ELEMENT MODEL DEVELOPMENT

Finite element numerical analysis was used to solve the three dimensional elasticity problem in order to determine stress and strain of the fiber, matrix or the overall composite specimen. The finite element method transforms the partial differential equations to a system of algebraic equations. The primary solution was obtained in terms of displacement. A solution post-processor subroutine converted the displacement solution into composite strain. The Kwon micromechanical method of cells provided the algorithm to solve for local cell strains, local cell stresses and composite stress. Stress values determined at the micromechanical cell level provided the dependent variable for stiffness reduction or failure relations. Details of the finite element method derivation are given below.

A. ANALYTICAL DERIVATION

The derivation for the force equilibrium equations of a three dimensional solid body which is experiencing negligible body forces is found in any advanced solid mechanics or elasticity textbook [Ref. 13, 14, 15, 16]. These equations are shown in Equation (2.1).

$$\begin{aligned}\frac{\partial \sigma_x}{\partial x} + \frac{\partial \tau_{xy}}{\partial y} + \frac{\partial \tau_{xz}}{\partial z} &= 0 \\ \frac{\partial \tau_{yx}}{\partial x} + \frac{\partial \sigma_y}{\partial y} + \frac{\partial \tau_{yz}}{\partial z} &= 0 \\ \frac{\partial \tau_{zx}}{\partial x} + \frac{\partial \tau_{zy}}{\partial y} + \frac{\partial \sigma_z}{\partial z} &= 0\end{aligned}\tag{2.1}$$

These three equilibrium equations are written in terms on nine stress variables. However, only six of the stress variables are independent due to the requirement for moment equilibrium. Application of moment equilibrium conditions on the unit solid element yields Equation (2.2).

$$\begin{aligned} \tau_{xy} &= \tau_{yx} \\ \tau_{xz} &= \tau_{zx} \\ \tau_{yz} &= \tau_{zy} \end{aligned} \tag{2.2}$$

The unit solid element is shown in Figure 2.1 below with stress terms as indicated to establish a reference for the sign convention and notation.

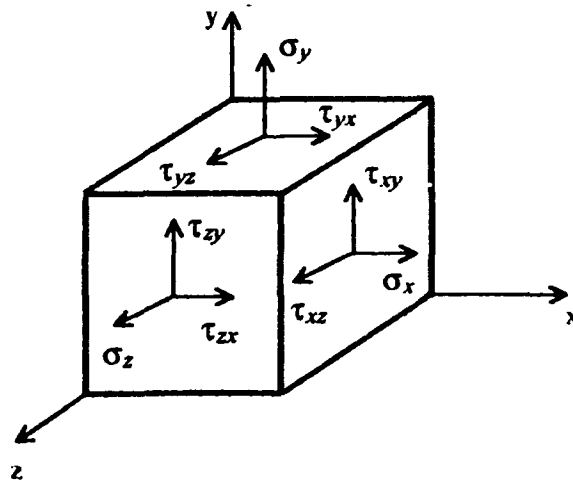


Figure 2.1 Unit Solid Cell With Stress Components

Let 'u', 'v', and 'w' represent displacement in the 'x', 'y', and 'z' directions respectively. Then, the relationship of strain to displacement, assuming small displacements, can be written as shown in Equation (2.3).

$$\begin{aligned} \epsilon_x &= \frac{\partial u}{\partial x} ; \quad \epsilon_y = \frac{\partial v}{\partial y} ; \quad \epsilon_z = \frac{\partial w}{\partial z} \\ \gamma_{xy} &= \left(\frac{\partial u}{\partial y} + \frac{\partial v}{\partial x} \right) ; \quad \gamma_{yz} = \left(\frac{\partial w}{\partial y} + \frac{\partial v}{\partial z} \right) ; \quad \gamma_{xz} = \left(\frac{\partial u}{\partial z} + \frac{\partial w}{\partial x} \right) \end{aligned} \quad (2.3)$$

The strain-displacement relations introduce six strain terms as unknown variables. Also, at this point, 'u', 'v', and 'w' are unknown. These equations can be written more conveniently in matrix form as in Equation (2.4).

$$\begin{Bmatrix} \epsilon_x \\ \epsilon_y \\ \epsilon_z \\ \gamma_{xy} \\ \gamma_{yz} \\ \gamma_{xz} \end{Bmatrix} = \begin{bmatrix} \frac{\partial}{\partial x} & 0 & 0 \\ 0 & \frac{\partial}{\partial y} & 0 \\ 0 & 0 & \frac{\partial}{\partial z} \\ \frac{\partial}{\partial y} & \frac{\partial}{\partial x} & 0 \\ 0 & \frac{\partial}{\partial z} & \frac{\partial}{\partial y} \\ \frac{\partial}{\partial z} & 0 & \frac{\partial}{\partial x} \end{bmatrix} \begin{Bmatrix} u \\ v \\ w \end{Bmatrix} \quad (2.4)$$

Next, consider the constitutive relationship between stress and strain of Equation (2.5).

$$\{ \sigma \} = [D] \{ \epsilon \} \quad (2.5)$$

In Equation (2.5), $\{\sigma\}$ is a '6 x 1' column vector of stress, $\{\epsilon\}$ is a '6 x 1' column vector of strain, and $[D]$ is the '6 x 6' matrix of material properties. Equations 2.1, 2.3, and 2.5 combine to give 15 equations with 15 unknown variables. Unfortunately, the equations include several partial differential equations.

The derivation of the finite element equations from the three dimensional elasticity equation above is based on course notes and commonly available current textbooks [Ref. 17, 18, 19, 20]. The method of weighted residuals as modified by Galerkin is employed to develop the displacement based finite element equations. Eight noded isoparametric rectangular parallelepiped elements are used for the formulation. Linear shape functions are used for analytical and computational simplicity. Detailed derivation according to these precepts is continued below.

The first step in converting the partial differential equations into algebraic equations is to apply the method of weighted residuals to the three dimensional stress equilibrium Equation (2.1). To this end, each of the three equations of Equation (2.1) are multiplied by a weight function, W_i ($i=1, 2, 3$), which is continuous over the physical domain of the problem. Then, the three new product equations are integrated over the entire problem domain. The goal is to choose weight functions W_i which are orthogonal to the initial residuals of the equilibrium equations such that the integral becomes equal to zero. If 'V' is the domain volume of the problem, the weighted residual equations are now shown in Equation (2.6).

$$\begin{aligned}
I_1 &= \iiint_V \left(\frac{\partial \sigma_x}{\partial x} + \frac{\partial \tau_{xy}}{\partial y} + \frac{\partial \tau_{xz}}{\partial z} \right) W_1 dV = 0 \\
I_2 &= \iiint_V \left(\frac{\partial \tau_{xy}}{\partial x} + \frac{\partial \sigma_y}{\partial y} + \frac{\partial \tau_{yz}}{\partial z} \right) W_2 dV = 0 \\
I_3 &= \iiint_V \left(\frac{\partial \tau_{xz}}{\partial x} + \frac{\partial \tau_{yz}}{\partial y} + \frac{\partial \sigma_z}{\partial z} \right) W_3 dV = 0
\end{aligned} \tag{2.6}$$

At this point it should be noted that boundary conditions must be specified for Equation (2.1). The boundary conditions may be specified as (1) essential or geometric boundary conditions where some surface displacements are specified, (2) natural or stress boundary conditions where surface tractions are specified, or (3) a combination of these types of boundary conditions. Before applying boundary conditions, further manipulation of the weighted residuals is required as shown by Equation (2.7): Integration by parts, commonly referred to as Gauss' theorem or the divergence theorem when applied in three dimensions, will be performed in order to weaken the continuity requirements on the approximate solution.

$$\begin{aligned}
I_1 &= \iiint_V \left[- \left(\sigma_x \frac{\partial W_1}{\partial x} + \tau_{xy} \frac{\partial W_1}{\partial y} + \tau_{xz} \frac{\partial W_1}{\partial z} \right) \right] dV + \iint_S (\sigma_x n_x W_1 + \tau_{xy} n_y W_1 + \tau_{xz} n_z W_1) dS \\
I_2 &= \iiint_V \left[- \left(\tau_{xy} \frac{\partial W_2}{\partial x} + \sigma_y \frac{\partial W_2}{\partial y} + \tau_{yz} \frac{\partial W_2}{\partial z} \right) \right] dV + \iint_S (\tau_{xy} n_x W_2 + \sigma_y n_y W_2 + \tau_{yz} n_z W_2) dS \\
I_3 &= \iiint_V \left[- \left(\tau_{xz} \frac{\partial W_3}{\partial x} + \tau_{yz} \frac{\partial W_3}{\partial y} + \sigma_z \frac{\partial W_3}{\partial z} \right) \right] dV + \iint_S (\tau_{xz} n_x W_3 + \tau_{yz} n_y W_3 + \sigma_z n_z W_3) dS
\end{aligned} \tag{2.7}$$

In Equation (2.7), 'S' is the domain surface boundary, 'V' is the domain volume, and 'n_x', 'n_y', and 'n_z' are outward unit surface normal directions cosines in the 'x', 'y', and 'z'

directions, respectively. Now, define the boundary stress conditions by surface tractions terms as shown in Equation (2.8):

$$\begin{aligned}\phi_x &= \sigma_x n_x + \tau_{xy} n_y + \tau_{xz} n_z \\ \phi_y &= \tau_{xy} n_x + \sigma_y n_y + \tau_{yz} n_z \\ \phi_z &= \tau_{xz} n_x + \tau_{yz} n_y + \sigma_z n_z\end{aligned}\quad (2.8)$$

Equation (2.7) can be written in matrix form with Equation (2.8) incorporated:

$$\iiint_V \begin{pmatrix} \sigma_x \frac{\partial W_1}{\partial x} + \tau_{xy} \frac{\partial W_1}{\partial y} + \tau_{xz} \frac{\partial W_1}{\partial z} \\ \tau_{xy} \frac{\partial W_2}{\partial x} + \sigma_y \frac{\partial W_2}{\partial y} + \tau_{yz} \frac{\partial W_2}{\partial z} \\ \tau_{xz} \frac{\partial W_3}{\partial x} + \tau_{yz} \frac{\partial W_3}{\partial y} + \sigma_z \frac{\partial W_3}{\partial z} \end{pmatrix} dV = \iint_S \begin{pmatrix} \phi_x n_x \\ \phi_y n_y \\ \phi_z n_z \end{pmatrix} dS \quad (2.9)$$

Equation (2.9) can be further modified by separating the column vector inside the volume integral into a product of a '3 x 6' matrix and a '6 x 1' vector. This step, shown in equation (2.10), isolates the weighting function derivatives in the matrix and the stress terms in the vector.

$$\begin{pmatrix} \sigma_x \frac{\partial W_1}{\partial x} + \tau_{xy} \frac{\partial W_1}{\partial y} + \tau_{xz} \frac{\partial W_1}{\partial z} \\ \tau_{xy} \frac{\partial W_2}{\partial x} + \sigma_y \frac{\partial W_2}{\partial y} + \tau_{yz} \frac{\partial W_2}{\partial z} \\ \tau_{xz} \frac{\partial W_3}{\partial x} + \tau_{yz} \frac{\partial W_3}{\partial y} + \sigma_z \frac{\partial W_3}{\partial z} \end{pmatrix} = \begin{pmatrix} \frac{\partial W_1}{\partial x} & 0 & 0 & \frac{\partial W_1}{\partial y} & 0 & \frac{\partial W_1}{\partial z} \\ 0 & \frac{\partial W_2}{\partial y} & 0 & \frac{\partial W_2}{\partial x} & \frac{\partial W_2}{\partial z} & 0 \\ 0 & 0 & \frac{\partial W_3}{\partial z} & 0 & \frac{\partial W_3}{\partial y} & \frac{\partial W_3}{\partial x} \end{pmatrix} \begin{pmatrix} \sigma_x \\ \sigma_y \\ \sigma_z \\ \tau_{xy} \\ \tau_{yz} \\ \tau_{xz} \end{pmatrix} \quad (2.10)$$

Substitution of the strain-displacement Equation (2.3) into the constitutive relation given by Equation (2.5) provides another useful identity as shown by Equation (2.11).

$$[D] \begin{Bmatrix} \frac{\partial u}{\partial x} \\ \frac{\partial v}{\partial y} \\ \frac{\partial w}{\partial z} \\ \frac{\partial u}{\partial y} + \frac{\partial v}{\partial x} \\ \frac{\partial v}{\partial z} + \frac{\partial w}{\partial y} \\ \frac{\partial w}{\partial x} + \frac{\partial u}{\partial z} \end{Bmatrix} = \begin{Bmatrix} \sigma_x \\ \sigma_y \\ \sigma_z \\ \tau_{xy} \\ \tau_{yz} \\ \tau_{xz} \end{Bmatrix} \quad (2.11)$$

Equation (2.4) is now substituted into the left hand side column vector of Equation (2.11).

Both Equation (2.10) and the modified Equation (2.11) are substituted into Equation (2.9)

to produce Equation (2.12).

$$\iiint_V \begin{bmatrix} \frac{\partial W_1}{\partial x} & 0 & 0 & \frac{\partial W_1}{\partial y} & 0 & \frac{\partial W_1}{\partial z} \\ 0 & \frac{\partial W_2}{\partial y} & 0 & \frac{\partial W_2}{\partial x} & \frac{\partial W_2}{\partial z} & 0 \\ 0 & 0 & \frac{\partial W_3}{\partial z} & 0 & \frac{\partial W_3}{\partial y} & \frac{\partial W_3}{\partial x} \end{bmatrix} [D] \begin{bmatrix} \frac{\partial}{\partial x} & 0 & 0 \\ 0 & \frac{\partial}{\partial y} & 0 \\ 0 & 0 & \frac{\partial}{\partial z} \\ \frac{\partial}{\partial y} & \frac{\partial}{\partial x} & 0 \\ 0 & \frac{\partial}{\partial z} & \frac{\partial}{\partial y} \\ \frac{\partial}{\partial z} & 0 & \frac{\partial}{\partial x} \end{bmatrix} \begin{Bmatrix} u \\ v \\ w \end{Bmatrix} dV = \iint_S \begin{Bmatrix} \phi_x n_x \\ \phi_y n_y \\ \phi_z n_z \end{Bmatrix} dS \quad (2.12)$$

Until this point, the elasticity relations have been manipulated to establish displacement as the variable for which to solve. Now, to discretize the problem for algebraic computational solution, assume that over a small domain each of the displacements can be represented by a polynomial. By discretizing a three dimensional domain, small-but-finite-sized volume elements can be formed. These finite elements become eight-noded. Each node can have three orthogonal displacements. Then, each element has a total of 24 degrees of freedom (dof). Calling 'u_i', 'v_i', and 'w_i' the displacement at each node, displacements can be defined in terms of polynomial shape functions as follows in Equation (2.13).

$$u = \sum_{i=1}^8 H_i u_i; \quad v = \sum_{i=1}^8 H_i v_i; \quad w = \sum_{i=1}^8 H_i w_i \quad (2.13)$$

Also, the first partial derivatives of the shape functions exist as shown in Equation (2.14).

$$\begin{aligned} \frac{\partial u}{\partial x} &= \sum_{i=1}^8 \frac{\partial H_i}{\partial x} u_i; & \frac{\partial v}{\partial x} &= \sum_{i=1}^8 \frac{\partial H_i}{\partial x} v_i; & \frac{\partial w}{\partial x} &= \sum_{i=1}^8 \frac{\partial H_i}{\partial x} w_i \\ \frac{\partial u}{\partial y} &= \sum_{i=1}^8 \frac{\partial H_i}{\partial y} u_i; & \frac{\partial v}{\partial y} &= \sum_{i=1}^8 \frac{\partial H_i}{\partial y} v_i; & \frac{\partial w}{\partial y} &= \sum_{i=1}^8 \frac{\partial H_i}{\partial y} w_i \\ \frac{\partial u}{\partial z} &= \sum_{i=1}^8 \frac{\partial H_i}{\partial z} u_i; & \frac{\partial v}{\partial z} &= \sum_{i=1}^8 \frac{\partial H_i}{\partial z} v_i; & \frac{\partial w}{\partial z} &= \sum_{i=1}^8 \frac{\partial H_i}{\partial z} w_i \end{aligned} \quad (2.14)$$

The '3 x 1' displacement vector can be expressed as the product of a '3 x 24' shape function matrix and a '24 x 1' nodal displacement vector as shown in Appendix A. The product of the '6 x 3' partial differential matrix of Equation (2.12) and the '3 x 24' shape

function matrix are typically combined into one '6 x 24' matrix. This matrix is referred to as the 'B' matrix in this development and the full 'B' matrix is also shown in Appendix A. In shorthand notation shown in Equation (2.15), the 'B' matrix can be partitioned into sub-matrices labelled 'B_i', where i=1 to 8 for eight sub-matrices.

$$[B] = [[B_1] [B_2] [B_3] [B_4] [B_5] [B_6] [B_7] [B_8]] \quad (2.15)$$

Based on this shorthand notation, the sub-matrices are defined in Equation (2.16).

$$[B_i] = \begin{bmatrix} \frac{\partial H_i}{\partial x} & 0 & 0 \\ 0 & \frac{\partial H_i}{\partial y} & 0 \\ 0 & 0 & \frac{\partial H_i}{\partial z} \\ \frac{\partial H_i}{\partial y} & \frac{\partial H_i}{\partial x} & 0 \\ 0 & \frac{\partial H_i}{\partial z} & \frac{\partial H_i}{\partial y} \\ \frac{\partial H_i}{\partial z} & 0 & \frac{\partial H_i}{\partial x} \end{bmatrix} \quad \text{where } i = 1 \text{ to } 8 \quad (2.16)$$

The Galerkin method (or more exactly the Bubnov-Galerkin method) takes the weighting functions as equivalent to the shape functions as shown in Equation (2.17).

$$W_1 = W_2 = W_3 = \begin{Bmatrix} H_1 \\ H_2 \\ H_3 \\ H_4 \\ H_5 \\ H_6 \\ H_7 \\ H_8 \end{Bmatrix} \quad (2.17)$$

Thus the Galerkin method only requires that the weighting function be continuous over small discrete intervals which correspond to the sides of the finite elements. Based on the Galerkin weighting functions shown above, the old weighting function matrix of Equation (2.12) can now be written in terms of the shape functions as per Equation (2.18).

$$\begin{bmatrix} \frac{\partial W_1}{\partial x} & 0 & 0 & \frac{\partial W_1}{\partial y} & 0 & \frac{\partial W_1}{\partial z} \\ 0 & \frac{\partial W_2}{\partial y} & 0 & \frac{\partial W_2}{\partial x} & \frac{\partial W_2}{\partial z} & 0 \\ 0 & 0 & \frac{\partial W_3}{\partial z} & 0 & \frac{\partial W_3}{\partial y} & \frac{\partial W_3}{\partial x} \end{bmatrix} = [B]^T \quad (2.18)$$

Thus, Equation (2.12) can be revised as shown in Equation (2.19).

$$\iiint_V [B]^T [D] [B] dV \{d\} = \iint_S \begin{Bmatrix} \phi_x \{H_i\} \\ \phi_y \{H_i\} \\ \phi_z \{H_i\} \end{Bmatrix} dS \quad (2.19)$$

In Equation (2.19), $\{d\}$ is the displacement vector which has grown from the original '3 x 1' vector of 'u', 'v', and 'w' to a '24 x 1' vector of terms 'u_i', 'v_i', and 'w_i'. Also, the right hand side surface integral '3 x 1' vector has a vector for each term and is simply shorthand for a '24 x 1' vector of discretized surface boundary tractions. The original three partial differential equations of elasticity equilibrium have now been reduced to a matrix equation of size 24. The integrals in Equation (2.19) may be easily solved if simple forms for shape functions are chosen and if the modelled section geometry is relatively simple.

If the modelled section geometry is complex, the finite element geometry can be made simple by employing a transform mapping to another reference space. In order to map 'x', 'y', and 'z' coordinates for an irregular shaped element onto 'r', 's' and 't' coordinates for a rectangular parallelepiped, the Jacobian transform matrix is required. The Jacobian transform matrix essentially scales each component of the original space to a new space. Thus, Equation (2.20) shows the Jacobian for an 'xyz' system mapped to an 'rst' system:

$$[J] = \begin{bmatrix} \frac{\partial x}{\partial r} & \frac{\partial y}{\partial r} & \frac{\partial z}{\partial r} \\ \frac{\partial x}{\partial s} & \frac{\partial y}{\partial s} & \frac{\partial z}{\partial s} \\ \frac{\partial x}{\partial t} & \frac{\partial y}{\partial t} & \frac{\partial z}{\partial t} \end{bmatrix} \quad (2.20)$$

In terms of the shape functions and the nodal points, the Jacobian is expressed in Equation (2.21) on the following page.

$$[J] = \begin{bmatrix} \sum_{i=1}^8 \frac{\partial H_i}{\partial r} x_i & \sum_{i=1}^8 \frac{\partial H_i}{\partial r} y_i & \sum_{i=1}^8 \frac{\partial H_i}{\partial r} z_i \\ \sum_{i=1}^8 \frac{\partial H_i}{\partial s} x_i & \sum_{i=1}^8 \frac{\partial H_i}{\partial s} y_i & \sum_{i=1}^8 \frac{\partial H_i}{\partial s} z_i \\ \sum_{i=1}^8 \frac{\partial H_i}{\partial t} x_i & \sum_{i=1}^8 \frac{\partial H_i}{\partial t} y_i & \sum_{i=1}^8 \frac{\partial H_i}{\partial t} z_i \end{bmatrix} \quad (2.21)$$

However, since the finite element integral equation includes shape function partial derivatives with respect to the 'xyz' coordinate system, the inverse of the Jacobian is required as described. Let $[J]^{-1} = [\Gamma]$, where $[\Gamma]$ is a '3 x 3' matrix. The shape function derivatives with respect to the 'xyz' system are now expressed in Equation (2.22) with respect to the 'rst' system.

$$\begin{aligned} \frac{\partial H_i}{\partial x} &= \Gamma_{11} \frac{\partial H_i}{\partial r} + \Gamma_{12} \frac{\partial H_i}{\partial s} + \Gamma_{13} \frac{\partial H_i}{\partial t} \\ \frac{\partial H_i}{\partial y} &= \Gamma_{21} \frac{\partial H_i}{\partial r} + \Gamma_{22} \frac{\partial H_i}{\partial s} + \Gamma_{23} \frac{\partial H_i}{\partial t} \\ \frac{\partial H_i}{\partial z} &= \Gamma_{31} \frac{\partial H_i}{\partial r} + \Gamma_{32} \frac{\partial H_i}{\partial s} + \Gamma_{33} \frac{\partial H_i}{\partial t} \end{aligned} \quad i = 1 \text{ to } 8 \quad (2.22)$$

Equation (2.22) is used to calculate the $[B]$ and $[B]^T$ matrices in the 'rst' system. Equation (2.21) is used to transform the volume differential. The finite element integral is transformed below as shown in Equation (2.23).

$$\iiint_V [B]^T [D] [B] dV(x,y,z) \{ d \} = \iiint_V [B]^T [D] [B] | J | dV(r,s,t) \{ d \} \quad (2.23)$$

The transformation to the 'rst' coordinate system results in simplified finite element integrals. The resultant transformed elements are termed isoparametric elements. The

term isoparametric refers to the equality between the degree of the equations for transforming 'xyz' into 'rst' coordinates and the degree of the shape functions for estimating displacement. The shape functions defined in terms of 'rst' system variables are shown in Equation (2.24).

$$\begin{aligned}
 H_1 &= \frac{1}{4}(1+r)(1+s)(1+t) \\
 H_2 &= \frac{1}{4}(1+r)(1-s)(1+t) \\
 H_3 &= \frac{1}{4}(1+r)(1-s)(1-t) \\
 H_4 &= \frac{1}{4}(1+r)(1+s)(1-t) \\
 H_5 &= \frac{1}{4}(1-r)(1+s)(1+t) \\
 H_6 &= \frac{1}{4}(1-r)(1-s)(1+t) \\
 H_7 &= \frac{1}{4}(1-r)(1-s)(1-t) \\
 H_8 &= \frac{1}{4}(1-r)(1+s)(1-t)
 \end{aligned}
 \tag{2.24}$$

In order to compute the integrals with a computer program, the Gauss quadrature of numerical integration is used. The volume integral is redefined as the triple summation from 1 to the number of integration points (NIP) of the integrand evaluated at Gauss integration points (r_i , s_i , and t_i) and multiplied by weighting factors as shown in Equation (2.25).

$$\iiint_V [B]^T [D] [B] |J| dV(r,s,t) \{d\} = \sum_{i=1}^{NIP} \sum_{j=1}^{NIP} \sum_{k=1}^{NIP} [B]^T [D] [B] |J| W_i W_j W_k \{d\}
 \tag{2.25}$$

The results of the numerical integration may vary over the elements in the domain of the model. Each of these results can be expressed as a '24 x 24' matrix which is termed the elemental stiffness matrix $[K_e]$.

Recall the surface traction boundary conditions from the right-hand side of Equation (2.12). The integration of the directional component of the applied stress over the element surface area of the applied stress is equal to the external force applied to the element. The result of the integration is a '24 x 1' vector $\{ F_e \}$ which is equivalent to the force in the 'x', 'y', and 'z' direction at each of the eight element nodes. Substituting these resultant terms into Equation (2.24) completes the finite element derivation which is shown in Equation (2.26).

$$[K_e] \{ d \} = \{ F_e \} \quad (2.26)$$

The finite element method involves combining these element matrix equations with given boundary conditions in order to form one large system of simultaneous equations for numerical solution. The computer programming methodology to achieve such a solution is described in the next section.

B. FORTRAN COMPUTER PROGRAM DEVELOPMENT

Finite element numerical analysis was accomplished using FORTRAN computer programs. The FORTRAN programs were implemented using the modular programming concepts and FORTRAN subroutines developed by Akin [Ref. 21]. The various FORTRAN programs used for this study differed from each other in only two or three subroutines out of approximately 55 subroutines to the main program.

Program housekeeping data, nodal coordinates, element-node connectivity, boundary conditions and material properties are read into the program from one input data file via

several standard Akin subroutines (for example, INPUT, INVECT, INPROP, and APLYBC). Efficient storage of the input data, interim calculated program data, and calculated results is accomplished through the use of semi-dynamic storage. Two large data vectors are sized in the main program to store fixed point and floating point data respectively. Matrix or array data is converted for storage in these column vectors. Computation of pointers to mark data locations in the column vectors does require some program overhead in that up to four subroutines (for example, PT1, PT2, PT3, and PT4A) are called for this purpose. However, the efficient use of computer core memory through the semi-dynamic storage method provides a significant advantage in the number of elements and nodes which can be used in the model.

Subroutine MODEL provides overall control for the rest of the program. All major subroutines are called from MODEL. Subroutine ASMMDS computes the element stiffness matrices using Gauss quadrature integration. (ASMMDS is a locally developed problem dependent subroutine). Two integration points are used in each coordinate direction at the element nodes. This results in eight independent integrations points per element. ASMMDS implements the subroutines (that is, MATER and COMDMX) which implement the Kwon micromechanical cell method to build the composite smeared properties. Fiber layup angle transformations are performed in subroutine STNROT. Finally, ASMMDS calls subroutine STORSQ to assemble the elemental stiffness matrices into the global stiffness matrix.

After completing ASMMDS computations, program control returns to MODEL where boundary conditions are applied, modifications are made to the global force column

vector and the global stiffness matrix (via subroutine APLYBC), and the displacement solution is obtained (in subroutines FACTOR and SOLVE). FACTOR uses the Cholesky method to factor the system square matrix into the product of a lower triangular matrix and its transpose. SOLVE use Cholesky-Gauss methods of forward and back substitutions to complete the solution. APLYBC, FACTOR and SOLVE are standard Akin subroutines.

Post-processing to calculate stress, strain, stiffness reduction or damage accumulation is accomplished in problem dependent subroutine MSTRES. MSTRES is an original subroutine developed and modified as required for this study. MSTRES re-computes the elemental stiffness matrices, and using the displacement solution previously obtained, implements the Kwon cell method to compute the micro-level cell strain from the composite macro-level strain. The micro-level cell strains are used to compute micro-level cell stresses and macro-level composite stresses. Stiffness reduction and damage criteria are applied based on the micro-level cell stresses calculated in this module. Program output is arranged from this module or from other standard Akin models as necessary.

Program iteration to modify material properties is required for computation of damage accumulation. Necessary iteration control is designed into control module MODEL for damage studies which are discussed later.

III STIFFNESS REDUCTION OF A CERAMIC MATRIX COMPOSITE

A. OVERVIEW

In a typical composite, the stiffness or Young's Modulus of the matrix is much less than that of the fiber. In polymer matrix composites (PMCs), the ratio of fiber stiffness to matrix stiffness may be on the order of 100. In ceramic matrix composites (CMCs), the ratio of fiber stiffness to matrix stiffness is usually on the order of 10 or lower. The ratio of fiber failure strength to matrix failure strength follows an analogous relationship as the stiffness ratios for PMCs and CMCs. Ceramic matrix materials are typically stiffer, stronger and more brittle than polymer matrix materials. However, PMCs tend to fail based on the stress and strain at the fiber level, while CMCs tend to fail based on relatively lower stresses and strains at the matrix level [Ref. 22]. Matrix cracking (or, more precisely, matrix micro-cracking) is one of the causes of initial failure of all composites, and, in particular, for CMCs. When the matrix develops cracks, the adjacent fibers must carry additional load. Thus, the effect of matrix cracking is seen on the macro-level as a reduction in stiffness for the composite structure.

Much previous research had been directed to model the matrix cracking phenomenon. Aveston and Kelly [Ref. 23] extended the models of the late 1960's for understanding the stress-strain behavior of composites with matrix cracks. They used rigorous shear-lag analysis to calculate the fiber stresses when the matrix cracks in a unidirectional fiber composite plate. They implement a "strain energy versus crack

growth" approach to relate the interfacial fiber-matrix shear stress to the unbonded matrix longitudinal stress after matrix cracking has occurred. Hahn and Tsai [Ref. 25] develop a bilinear model to explain stress-strain behavior before and after matrix cracking. Hahn and Tsai developed their model with experimental results for a $[0^\circ/90^\circ]$, glass fiber, epoxy matrix composite loaded in a uni-stress condition. Garrett and Bailey [Ref. 25] and Parvizi et al. [Ref. 26] tested cross-ply glass fiber, polyester matrix composite materials to observe matrix cracking. They validated some of the earlier theoretical work of Aveston and Kelly. They also studied the effect of applied stress and matrix crack spacing. Reifsnider and his team [Ref. 27] identified a matrix crack pattern in terms of a Characteristic Damage State related to applied stress and based on their experimental work with composite laminates with multiple fiber layup angles. Talreja [Ref. 28, 29] uses a complex, rigorous continuum mechanics approach to derive constitutive relations which essentially extends the work of the authors cited above. However, Talreja's approach is based on factors adjusted by a curve-fitting to experimental results. Talreja's method provides some insight into the stiffness reduction from matrix cracking but implementation of his model requires significant experimental data.

This research attempts to extend the prior studies by developing a correlation for composite stiffness reduction due to matrix cracking. The correlation is based on results from simple tensile testing of a composite specimen. The tensile testing provides characterization of stiffness reduction versus applied load. While this correlation approach is not predictive from first principles and basic material properties, it provides a

methodology to predict global structural behavior of a composite material to the micro-level stresses in the fiber and matrix.

B. EXPERIMENTAL BASIS

Wang [Ref. 30] performed comprehensive testing on continuous Nicalon (SiC) fiber reinforced calcium aluminosilicate (CAS) composite systems. Wang focused much attention on standardization of specimen design and testing methodology due to lack of standards for testing fiber reinforced ceramic composites. Manufacturer supplied data for the fiber and matrix are indicated in Table 3.1 below.

TABLE 3.1 CHARACTERISTICS OF MATRIX AND FIBERS IN THE SiC/CAS COMPOSITES

Properties	CAS Matrix	Nicalon, SiC Fibers
Elastic Modulus (GPa)	98	193.2
Tensile Strength (MPa)	124	2760
Poisson's Ratio	0.255	Not Provided

Wang determined the following properties for a 36% fiber volume SiC/CAS unidirectional composite: Elastic Modulus ranged from 124 to 131 GPa and Poisson's ratio ranged from 0.29 to 0.30. These values agree with results of the micromechanical model.

Wang performed uniaxial cyclic loading of unidirectional [0], [0₃/90/0₃], and [0₃/90₃/0₃] composites. Stiffness reduction results of these tests are used for this study.

C. MATRIX STIFFNESS REDUCTION CORRELATION

Kwon and Berner [Ref. 31] proposed the following method to account for the effect of matrix cracking on the composite stiffness. The degradation of the matrix elastic modulus is assumed to be a function of the micro-level matrix stress as shown in Equation (3.1).

$$E^m = E_o^m f(\sigma_{ij}^m) \quad (3.1)$$

In Equation (3.1), the superscript 'm' represents a matrix property, the subscript 'o' represents the original undamaged elastic modulus, and 'f' is a stiffness degradation function which depends on the matrix cell stresses. A Weibull type distribution function of the matrix cell von Mises stress values is used to model the stiffness degradation of the matrix. The stiffness degradation Weibull function is given in Equation (3.2).

$$f = \begin{cases} \exp \left[-\gamma \left(\frac{\sigma_{vme}^m - \sigma_{ys}^m}{\sigma_{ys}^m} \right)^\beta \right] & \text{if } \sigma_{vme}^m > \sigma_{ys}^m \\ 1 & \text{if } \sigma_{vme}^m \leq \sigma_{ys}^m \end{cases} \quad (3.2)$$

In Equation (3.2), σ_{vme}^m is the equivalent von Mises stress of the matrix, σ_{ys}^m is the yield or failure strength of the matrix, and γ and β are constants of the material which are determined from experiment.

A one-eighth model of a tensile test specimen was developed for input into an FEM program developed as described in Chapter II. The composite model consisted of two layers of 20 elements for a total of 40 elements. Material properties from Table 3.1, CAS matrix Poisson's ratio of 0.31, and fiber volume of 36% were input for the analysis. A

CAS matrix yield stress value of 130 MPa was used for the stiffness reduction function. Boundary conditions of known displacements which were derived from the Wang experimental strain and composite stiffness reduction data were also input into the FEM program. The FEM postprocessor determined the matrix and fiber cell stresses. The matrix von Mises level stress values were calculated at the cell level and then averaged throughout the model. Average matrix cell level von Mises stress values were considered valid as the specimen was modelled for uniaxial displacement loading. A separate FORTRAN program based on the Kwon micromechanical model as implemented by subroutine COMDMX was run to correlate the matrix stiffness reduction to the composite stiffness reduction. This step essentially was directed at determining what the required level of matrix stiffness degradation would be for a given composite stiffness degradation. At this point, necessary information to perform a correlation was accumulated. This data is displayed in Table 3.2. Next, Equation (3.2) was manipulated (using logarithms and basic algebra) into the format required to perform a least squares fit for constants γ and β . The least square fit constants were used to calculate the reduced matrix stiffness in order to finally compute the new predicted, reduced composite stiffness. This predicted, reduced composite stiffness was correlated to the experimentally determined, reduced composite stiffness. The least square fit constants were adjusted to optimize the maximum error and the root mean square error between the predicted and experimental, reduced composite stiffness values. These steps were performed using a Microsoft Excel 4.0 spreadsheet, its built-in functions, and an interactive "macro" or program.

TABLE 3.2 STIFFNESS REDUCTION CURVE FIT DATA

Strain (experimental)	% Stiffness Reduction (experimental)	E_c Multiplier (calculated)	Required E_m Multiplier (computed)	Matrix von Mises Stress (MPa) (computed)
0.0015	1.5%	0.985	0.968	147
0.0020	4.0%	0.960	0.915	196
0.0025	12.5%	0.875	0.736	245
0.0030	18.0%	0.820	0.620	294
0.0035	22.5%	0.775	0.525	343
0.0040	24.5%	0.755	0.483	392
0.0045	26.0%	0.740	0.452	441
0.0050	28.5%	0.715	0.398	490
0.0055	32.0%	0.680	0.325	539

From the above data and analysis, γ was determined to equal 0.307 and β was determined to equal 1.16. These material constants were assumed to be independent of the composite layer configuration, the material properties of the fiber, and the volume fraction of the fiber.

D. FEM STIFFNESS REDUCTION RESULTS

The correlation for stiffness reduction discussed above was incorporated into the computer FEM program. To achieve stiffness reduction, the program was run once with initial undamaged material properties to determine the matrix micromechanical stress values. The matrix stiffness reduction factor was calculated based on these stress values.

The matrix properties were degraded accordingly, and the FEM program was re-run to determine the final specimen displacement and strain with the matrix cracking damage present. Two different laminates were studied: Two cross-ply composite laminates made of SiC/CAS with a fiber volume of 36%. Numerical results were compared with Wang's experimental results as shown in Figures 3.1, 3.2, and 3.3. The numerical method for the cross-ply $[0_3/90/0_3]$ composite predicts slightly lower stiffness reduction at low composite strains and slightly higher stiffness reduction at medium-to-high composite strains than that obtained by experiment. For the cross-ply $[0_3/90_3/0_3]$ composite, the numerical method significantly under-predicts the stiffness reduction as compared to the experimental results. In the latter case, post-experiment composite analysis indicated some fiber breakage in addition to the matrix cracking phenomenon. The fiber breakage offers a partial explanation for the higher than predicted stiffness reduction. Also, other non-modelled micro-level stresses or load transfer mechanisms might account for the additional stiffness reduction.

To gain further insight into the stiffness reduction mechanism for the cross-ply composite laminates, the percent stiffness reduction was plotted for matrix cracking in each layer and for matrix cracking in the whole laminate. Figures 3.4 and 3.5 display these plots. One might expect a greater degree of matrix cracking to occur in the 90° layer, as its matrix supports a majority of the stress which results from the applied longitudinal load than does its fibers. But, for the $[0_3/90/0_3]$ composite, most stiffness reduction occurred due to matrix cracks in the 0° layer. The reason is that the 0° layer is much thicker than the 90° layer. As a result, the 0° layer carries more load compared

to the 90° layer. For the $[0_3/90_3/0_3]$ composite, the numerical method indicates that stiffness reduction due to matrix cracking in both layers is comparable. The relatively thick 90° layer in $[0_3/90_3/0_3]$ yielded more contribution to the stiffness degradation, due to matrix cracking in the 90° layer, than the relatively thin 90° layer in $[0_3/90/0_3]$.

Figures 3.6, 3.7, and 3.8 display the longitudinal fiber stress changes as the matrix cracking is modelled. For all composite laminates considered, as the matrix cracks, the fiber stress is increased due to load transfer from damaged matrix to the relatively stiff longitudinal fibers. For the cross-ply $[0_3/90/0_3]$ laminate of Figure 3.7, matrix cracking in the 0° layer accounts for most of the stress increase in the longitudinal fibers. For the cross-ply $[0_3/90_3/0_3]$ laminate of Figure 3.8, matrix cracking in either layer contributes approximately the same relative share of longitudinal fiber stress increase. These fiber stress graphical results further indicate the utility of the Kwon cell method.

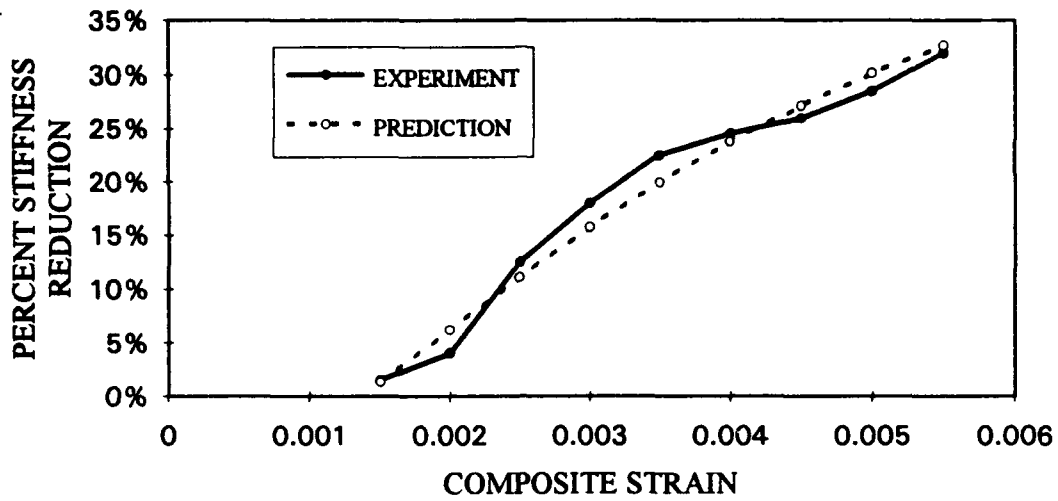


Figure 3.1 Experimental And Predicted Stiffness Reduction Due To Matrix Cracking For A Unidirectional SiC/CAS Composite Laminate Loaded Uniaxially.

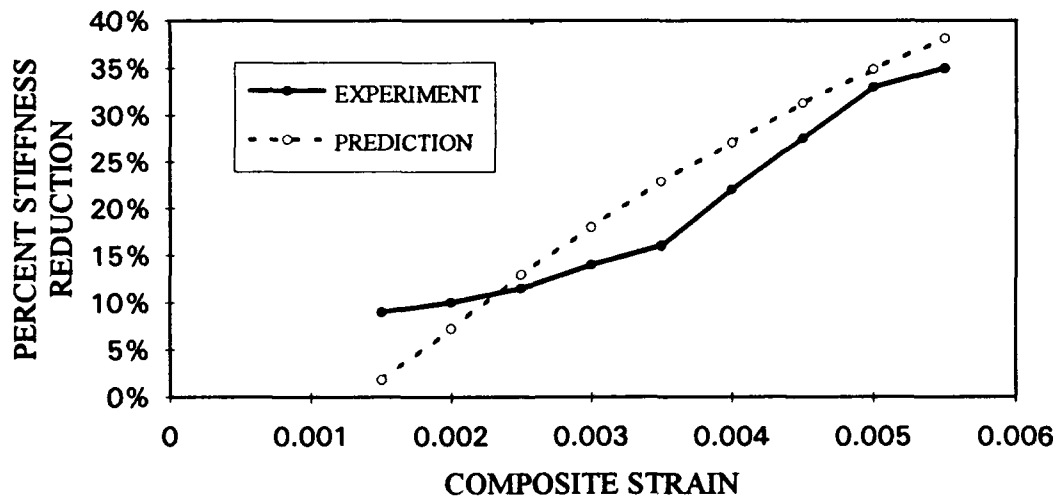


Figure 3.2 Experimental And Predicted Stiffness Reduction Due To Matrix Cracking For A [0₃/90/0₃] SiC/CAS Composite Laminate Loaded Uniaxially.

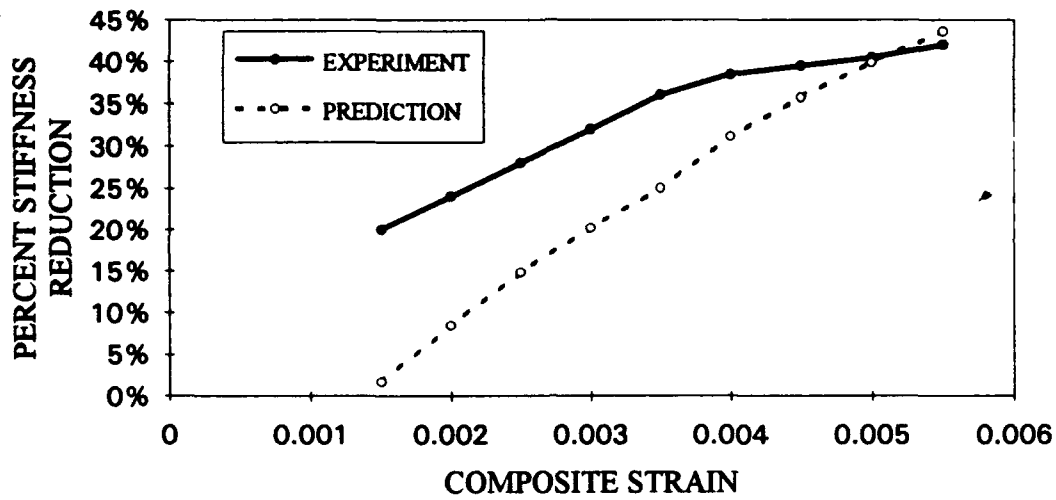


Figure 3.3 Experimental And Predicted Stiffness Reduction Due To Matrix Cracking For A $[0_3/90_3/0_3]$ SiC/CAS Composite Laminate Loaded Uniaxially.

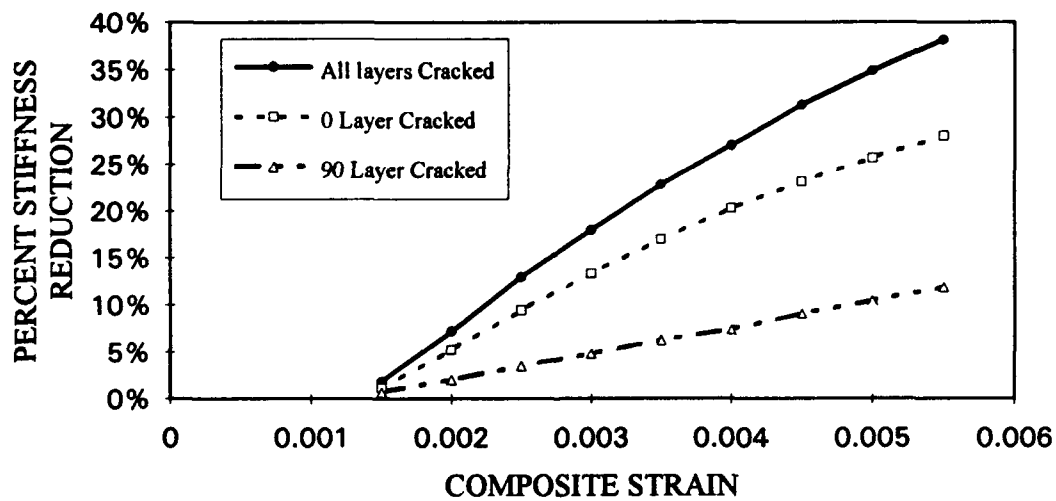


Figure 3.4 Stiffness Reduction Due To Matrix Cracking In Different Layers Of A $[0_3/90_3/0_3]$ SiC/CAS Composite Laminate Loaded Uniaxially.

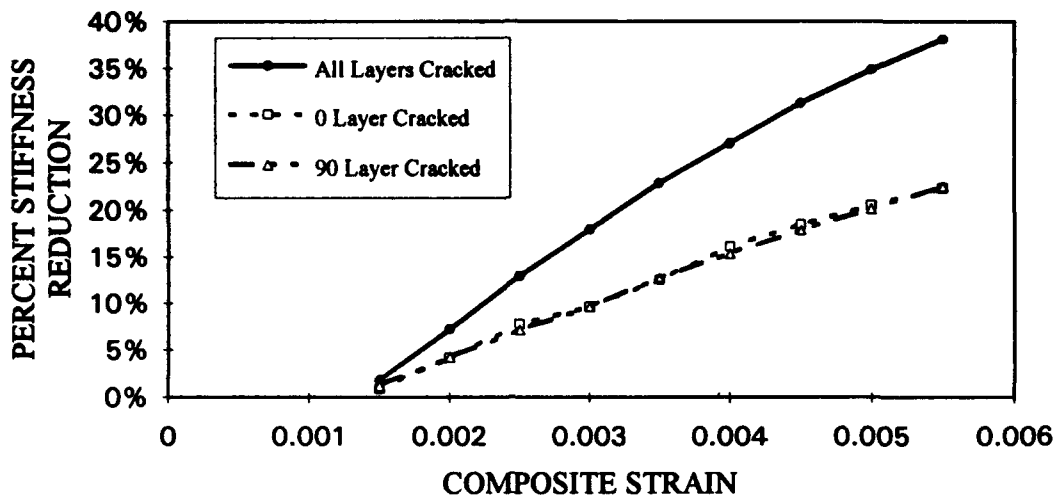


Figure 3.5 Stiffness Reduction Due To Matrix Cracking In Different Layers Of A $[0_3/90_3/0_3]$ SiC/CAS Composite Laminate Loaded Uniaxially.

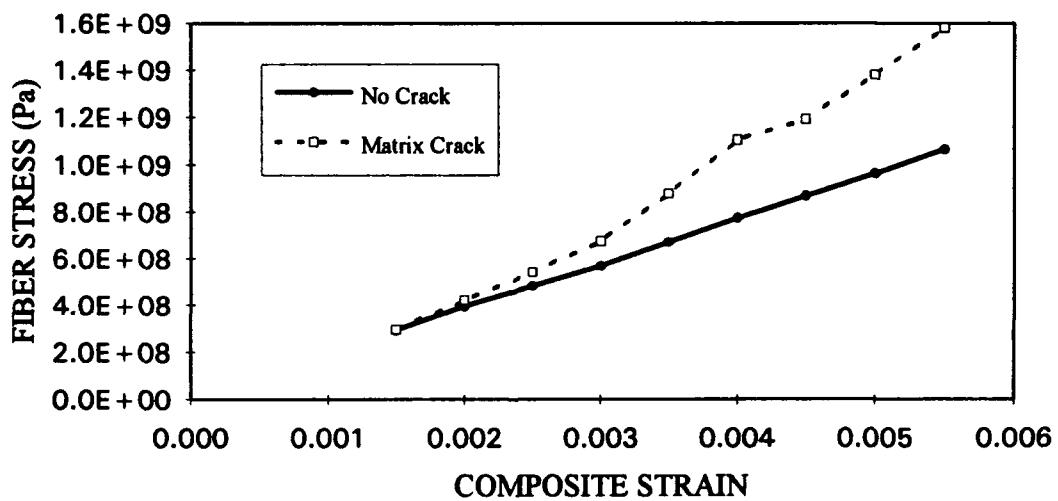


Figure 3.6 Effects On Longitudinal Fiber Stress Of Stiffness Reduction Due To Matrix Cracking Of A Unidirectional SiC/CAS Composite Laminate Loaded Uniaxially.

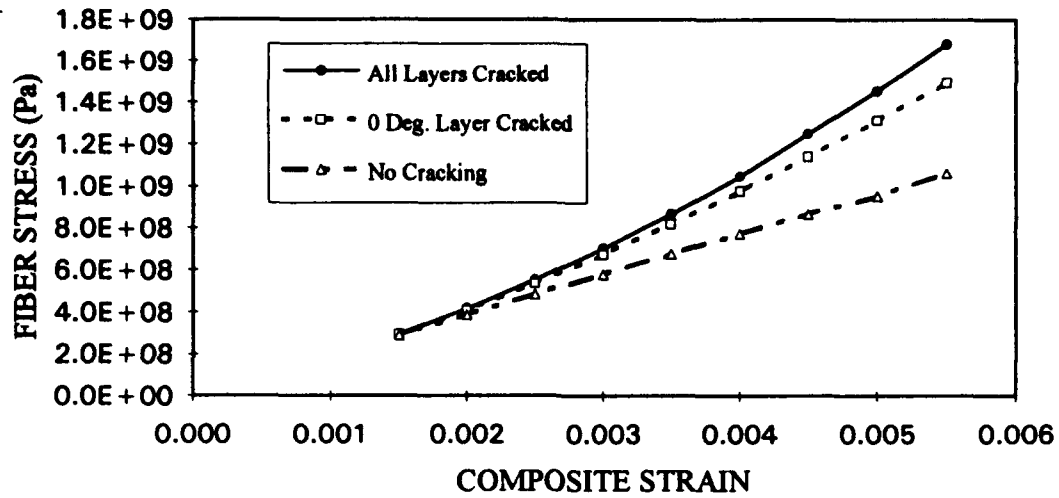


Figure 3.7 Effects On Longitudinal Fiber Stress Of Stiffness Reduction Due To Matrix Cracking In Different Layers Of A $[0_3/90_3/0_3]$ SiC/CAS Composite Laminate Loaded Uniaxially.

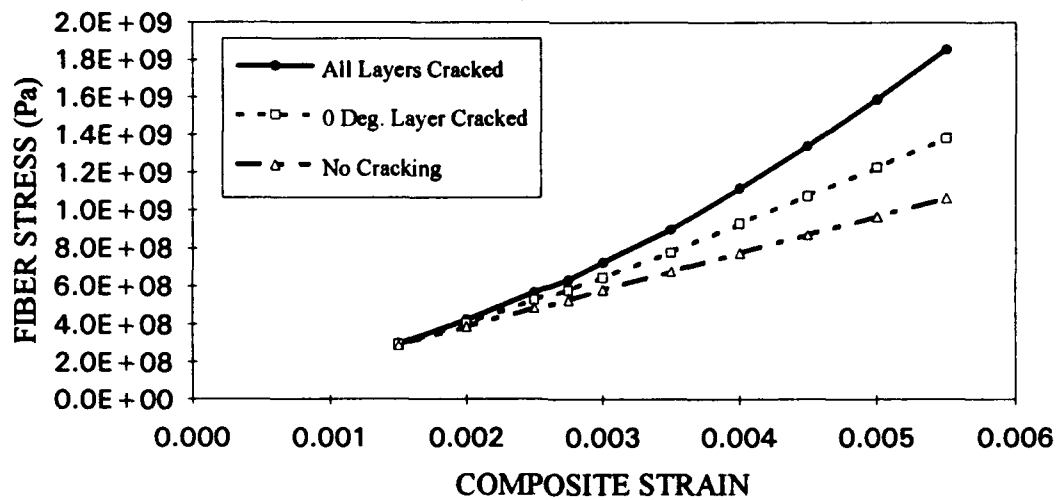


Figure 3.8 Effects On Longitudinal Fiber Stress Of Stiffness Reduction Due To Matrix Cracking In Different Layers Of A $[0_3/90_3/0_3]$ SiC/CAS Composite Laminate Loaded Uniaxially.

E. PARAMETRIC STUDY

A parametric study for different fiber volumes in a unidirectional SiC/CAS composite laminate was conducted and reported by Kwon and Berner [Ref. 32]. Results for stiffness reduction sensitivity to the variation of fiber volume are indicated in Figure 3.9. As the magnitude of the applied strain boundary condition was increased, the fiber stress also increased. This resulted in an increased matrix stress too. When matrix stress increased, the stiffness reduction factor also increased. Thus, composite stiffness reduction increased for all fiber volumes modelled when the strain was increased. At higher fiber volumes, the numerical model indicated smaller stiffness reduction. This result is expected: As the amount of fibers was increased, the share of load carried by the fibers increased likewise. Thus, local matrix stress and subsequent matrix cracking was decreased.

Figure 3.10 indicates the longitudinal fiber stress versus strain for several different fiber volume fractions. The fiber stress increases with strain due to increasing load transfer from the damaged matrix to the undamaged fibers. As the effect of matrix cracking is reduced with higher fiber volumes, the rate of increase of fiber stress goes down.

The parametric study results appear reasonable. However, comparison with experimental data is warranted to fully validate the results. Also, experimental verification could substantiate the assumption that the stiffness reduction correlation, developed in section 'C' above, is truly independent of the fiber volume.

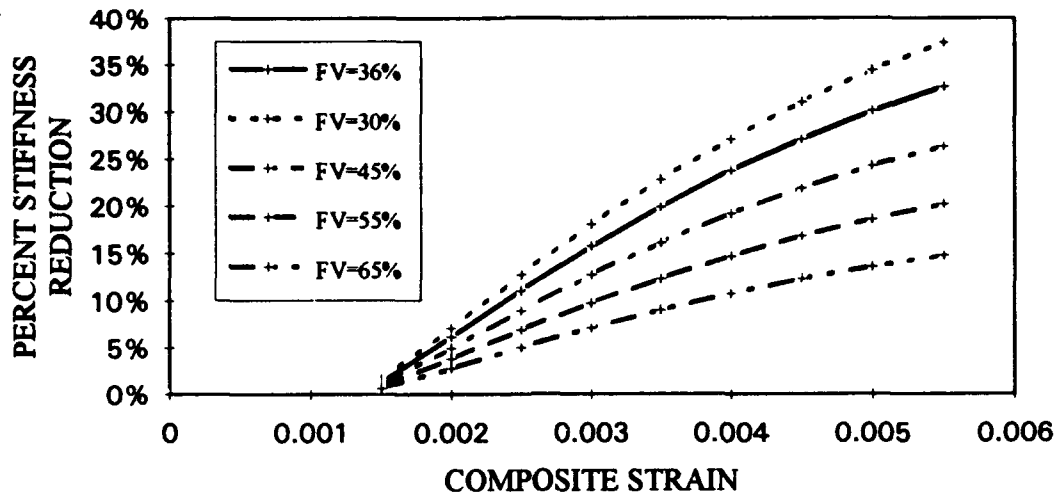


Figure 3.9 Stiffness Reduction Versus Strain For Different Fiber Volumes For A Unidirectional SiC/CAS Composite Laminate.

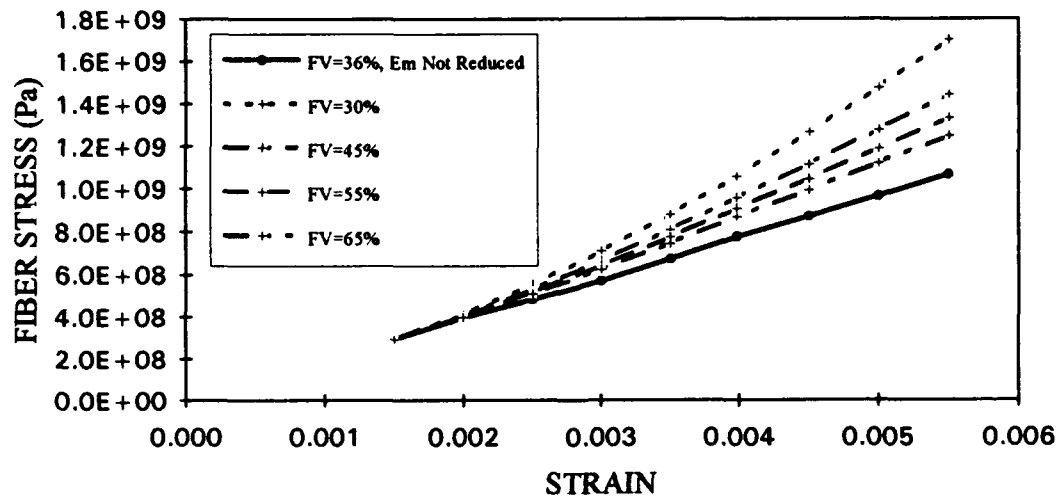


Figure 3.10 Longitudinal Fiber Stress Versus Strain For Different Fiber Volumes For A Unidirectional SiC/CAS Composite Laminate.

IV. STIFFNESS REDUCTION MODIFIED BY THERMAL RESIDUAL STRESS

A. BACKGROUND

The mismatch between the coefficient of thermal expansion (CTE) for the fiber and the matrix of ceramic matrix composites (CMCs) and the relatively high fabrication temperatures for CMCs can cause significant residual thermal stresses. These residual thermal stresses may have a significant effect on the performance of CMCs.

The micromechanical matrix stress was the primary factor in the stiffness reduction correlation developed for the SiC/CAS as discussed in the previous chapter. The Weibull type correlation has a reasonable physical basis in using the ratio of the difference of matrix cell stress and matrix yield stress to the matrix yield stress: This ratio indicates some sort of threshold matrix cell stress level at which the matrix begins to develop cracks. Residual thermal stresses in the matrix could affect the threshold stress for the onset of cracking.

A calculation was performed to estimate the residual thermal stresses in the SiC/CAS composite laminates which were analyzed in Chapter III. The calculated thermal residual stress terms were incorporated into the FEM program for the analysis of stiffness reduction. Results of the numerically predicted stiffness reduction were compared with experimental data.

B. DERIVATION

Two separate calculations were performed for the thermal residual stress in the matrix of the SiC/CAS composites: unidirectional laminate calculations and cross-ply laminate calculations. The coefficient of thermal expansion (CTE) for the SiC fiber, α_f , was taken as 4.0×10^{-6} per degree Celsius; the CTE for the CAS matrix, α_m , 5.0×10^{-6} per degree Celsius. This data is based on Wang [Ref. 30]. Other basic material properties listed previously in Table 3.1 were also used. A temperature delta of 300°C was used as a typical value for the difference between fiber/matrix bond setting fabrication temperature to application temperature. The approximate computation described below relies on the Chamis relations [Ref. 3] to determine smeared properties for the composite laminates. A method to numerically compute the thermal residual stresses using the Kwon cell method is briefly outlined in Appendix B.

1. Unidirectional Case

Consider a two dimensional view of the fiber and matrix interface as two solid blocks which are adjacent to one another. A force balance must exist between the bonded fiber and matrix after cooldown from bond setting during fabrication as shown in Equation (4.1).

$$\sigma_f A_f = \sigma_m A_m \quad (4.1)$$

If each side of Equation (4.1) is multiplied by the composite thickness and then divided by the total composite volume, Equation (4.2) is obtained.

$$\sigma_f V_f = \sigma_m V_m \quad (4.2)$$

The mechanical strain of the fiber and matrix is given by the basic Hooke's Law relationship and is equal to the respective elastic modulus divided by the respective stress term. The thermal strain is equal to the appropriate CTE times the temperature delta. Equation (4.3) shows that the sum of the mechanical strains of the fiber and the matrix must be equal to the magnitude of the difference of the thermal strains of the matrix and the fiber.

$$\frac{\sigma_f}{E_f} + \frac{\sigma_m}{E_m} = |\alpha_m - \alpha_f| \Delta T \quad (4.3)$$

When Equations (4.2) and (4.3) are combined algebraically, Equation (4.4) results.

$$\sigma_m = \frac{|\alpha_m - \alpha_f| \Delta T}{\frac{1}{E_m} + \frac{V_m}{E_f V_f}} \quad (4.4)$$

Although developed independently, Equation (4.4) is equivalent to the result derived by Sambell, et. al., [Ref. 33]. When the appropriate values are substituted into Equation (4.4), the resultant residual thermal stress in the matrix is approximately 15 MPa.

2. Cross-Ply Case

The cross-ply development for thermal residual stress is analogous to the unidirectional development, but necessarily more complex due to the consideration of the two laminae of different fiber layup angle and the two stress directions. In the following derivation, subscript 'L' represents the global longitudinal direction, subscript 'T' represents the global transverse direction, superscript '0' represents the 0° fiber layup lamina, and

superscript '90' represents the 90° fiber layup lamina. Four different strain terms are represented in Equation (4.5).

$$\begin{aligned}
 \varepsilon_L^{90} &= \frac{\sigma_L^{90}}{E_L^{90}} - \nu_{LT} \frac{\sigma_T^{90}}{E_T^{90}} + \alpha_L^{90} \Delta T \\
 \varepsilon_T^{90} &= \frac{\sigma_T^{90}}{E_T^{90}} - \nu_{TL} \frac{\sigma_L^{90}}{E_L^{90}} + \alpha_T^{90} \Delta T \\
 \varepsilon_L^0 &= \frac{\sigma_L^0}{E_L^0} - \nu_{LT} \frac{\sigma_T^0}{E_T^0} + \alpha_L^0 \Delta T \\
 \varepsilon_T^0 &= \frac{\sigma_T^0}{E_T^0} - \nu_{TL} \frac{\sigma_L^0}{E_L^0} + \alpha_T^0 \Delta T
 \end{aligned}
 \tag{4.5}$$

Because the strains in the global transverse and longitudinal directions must be equal, Equation (4.5) actually represents two independent equations with four unknowns. To add two required equations to the system, Equation (4.6) describes the force balance between the laminae.

$$\begin{aligned}
 A^0 \sigma_L^0 + A^{90} \sigma_T^{90} &= 0 \\
 A^0 \sigma_T^0 + A^{90} \sigma_L^{90} &= 0
 \end{aligned}
 \tag{4.6}$$

To solve for the longitudinal and transverse CTE values and elastic modulus values for the fiber, the equation of Chamis [Ref. 3] were used. The matrix CTE was assumed to be isotropic. Noting that the ratio of the areas for the 0° lamina to the 90° lamina is two for the [0₃/90₃/0₃] composite and six for the [0₃/90/0₃] composite, the system of four equations and four unknowns given by Equations (4.5) and (4.6) is solved to give residual thermal stress values. Matrix thermal residual stress values are shown in Table 4.1.

TABLE 4.1 MATRIX THERMAL RESIDUAL STRESSES

Lamina	[0 ₃ /90 ₃ /0 ₃] Laminate Matrix Thermal Residual Stress (MPa)		[0 ₃ /90/0 ₃] Laminate Matrix Thermal Residual Stress (MPa)	
	σ_1	σ_2	σ_1	σ_2
0°	-19.3	25.3	-8.43	10.6
90°	-40.8	52.1	-47.3	68.3

C. FEM STIFFNESS REDUCTION WITH THERMAL RESIDUAL STRESS

The Weibull stiffness reduction function constants were re-computed using the matrix residual stress values. The new γ was 0.238 and the new β was 1.42. Figure 4.1 shows the graph for the stiffness reduction of the unidirectional composite laminate. The new predicted stiffness reduction values show good agreement with the experimental results, but the overall comparison indicates mixed results for this case. The new predicted stiffness reduction values show slight improvement over the previous (without thermal residual stress) predicted values at low strains. The previous model shows slightly better agreement with experimental results at medium to high strain rates. Both predictions are within the same range of accuracy for the constants and assumptions employed in deriving the model.

Figure 4.2 shows the graph of stiffness reduction for the cross-ply [0₃/90/0₃] composite laminate. The new predicted stiffness reduction values show vastly improved

agreement with experimental results as compared to the previous model. For medium to high strains, the new predicted values are extremely close to the experimental values. For low strain levels the predicted stiffness reduction due to matrix cracking is smaller than both the experimental results and the previous results. However, the shape of the stiffness reduction curve shows upward curvature and then levels off just short of achieving downward curvature. This type of behavior might occur if weak fibers in the composite laminate were cracked or damaged at a low strain level. From a statistical viewpoint, some early weak fiber breakage is a real probability.

Figure 4.3 shows the graph of stiffness reduction with thermal residual stress for the cross-ply $[0_3/90_3/0_3]$ composite. The numerical prediction with thermal residual stress incorporated shows slight improvement in matching the experimental results as the previous numerical method. These results indicate the need for further refinement of the stiffness reduction correlation for thermal residual stresses and their effect on matrix cracking.

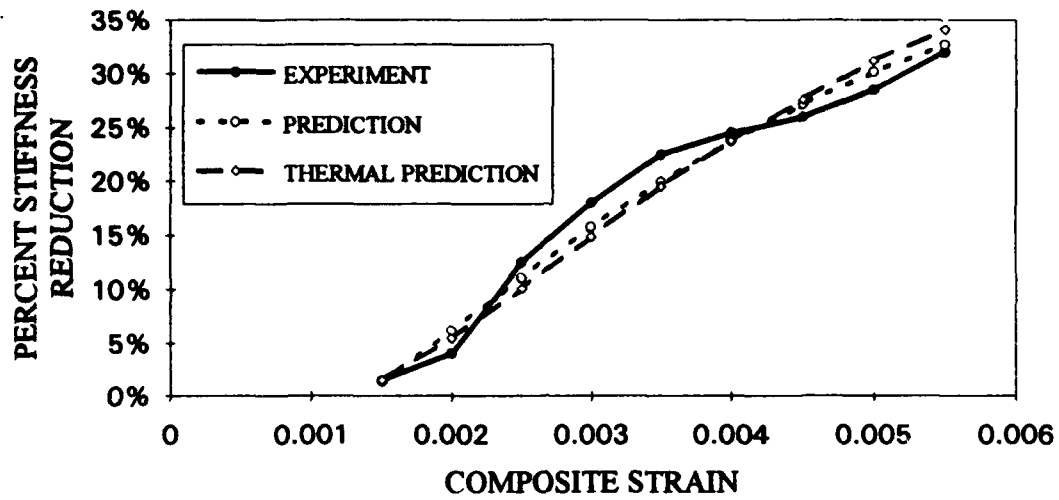


Figure 4.1 Experimental And Predicted Stiffness Reduction Due To Matrix Cracking For A Unidirectional SiC/CAS Composite Laminate Loaded Uniaxially.

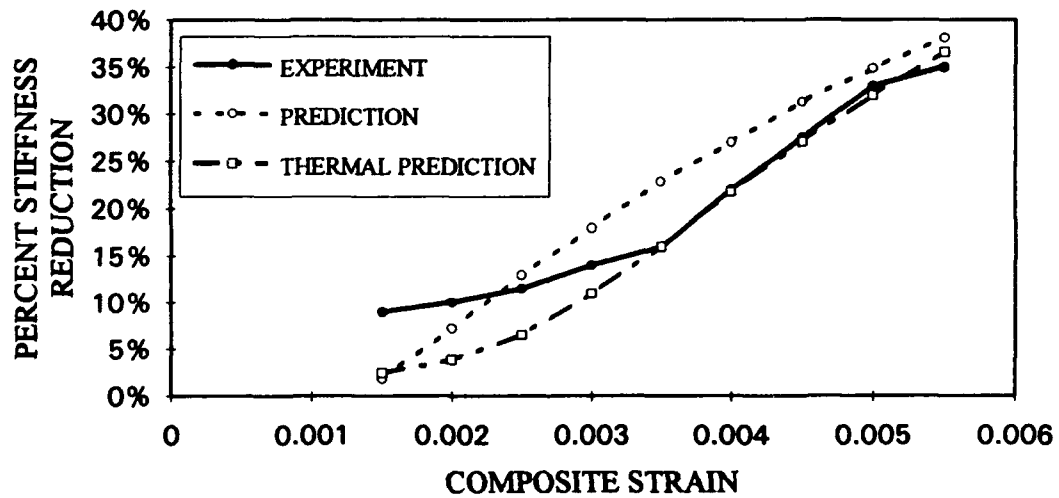


Figure 4.2 Experimental And Predicted Stiffness Reduction Due To Matrix Cracking For A $[0_3/90/0_3]$ SiC/CAS Composite Laminate Loaded Uniaxially.

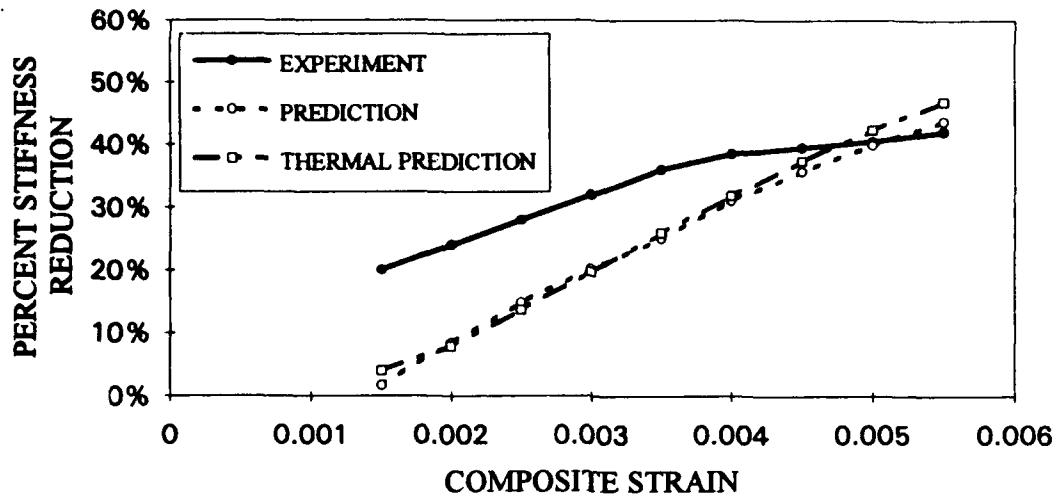


Figure 4.3 Experimental And Predicted Stiffness Reduction Due To Matrix Cracking For A $[0_3/90_3/0_3]$ SiC/CAS Composite Laminate Loaded Uniaxially.

V. DAMAGE PROGRESSION AND FAILURE IN A POLYMER MATRIX COMPOSITE

A. OVERVIEW

A finite element analysis was also performed concerning the effects of flaws (in this case, a circular hole) on the failure behavior of composite laminates. From classical elasticity based on isotropic materials, an "infinite" plate containing a small circular hole and loaded in uniaxial tension, " σ_0 ," will experience a stress concentration factor (SCF) at the edge of the hole. The SCF produces a stress of magnitude 3 times σ_0 in a region outside the hole and perpendicular to the applied stress. Konisch and Whitney [Ref. 34] noted that the classical SCF approach produced anomalous results when applied to composite laminates with holes. They modified a solution to the elasticity equations for an isotropic material for application to a composite plate with a hole. Then, using a semi-inverse solution technique, they determined the stresses in the vicinity of the hole. Their semi-inverse solution produced a slightly improved correlation with experimental data. However, overall force equilibrium was not satisfied throughout the composite by this type of semi-inverse solution.

The study of stress around holes in composite plates is predicated by the need to use bolted or pinned joints to connect such plates within structures. Bolt hole analysis has added complexity due to the loading in the hole area. Chang, Scott and Springer

[Ref. 35, 36] studied the failure of such joints in composite materials. They developed models for the bolt hole boundary conditions and implemented a variation of the Yamada and Sun [Ref. 37] failure criteria. The Yamada-Sun criteria is a quadratic equation for composite laminate failure prediction based on average laminate properties. More recently, Chang and Chang have extended the early work to study the failure of composite plates with non-loaded holes [Ref. 38]. The recent Chang research is based upon FEM analysis using composite laminate theory. Chang used statistical Weibull functions to determine degraded stiffness properties for the composite laminate when composite damage criteria are exceeded. Chang implemented a fiber damage zone failure method covered by Hahn and Tsai [Ref. 39]. The Chang numerical predictions show good agreement with experimental results. This current work attempts to similarly predict failure progression using the Kwon micromechanical model with its strong physical basis in the micromechanical properties of the composite constituents. Further finite element analysis and modelling remain to fully compare this present method with Chang's results.

B. FAILURE CRITERIA AND MODELLING

Chang implemented failure criteria at the composite level using modifications of the quadratic relations of Yamada and Sun. Since material failure has physical origins at the micromechanical level, it is desirable to establish failure criteria on material properties at that level. Aboudi [Ref. 8] has proposed the criteria presented in Equations (5.1) and (5.2).

$$|\sigma_{11}^f| \leq X_f \quad (5.1)$$

$$\left(\frac{\sigma_{22}^m}{X_m}\right)^2 + \left(\frac{\sigma_{12}^m}{S_m}\right)^2 \leq 1 \quad (5.2)$$

In Equation (5.1), σ_{11}^f is the local fiber longitudinal stress and X_f is the ultimate tensile strength of the fiber in the longitudinal direction. In Equation (5.2), σ_{22}^m is the local transverse stress of the matrix, σ_{12}^m is the local matrix shear stress in the longitudinal-transverse plane, X_m is the ultimate tensile strength of the matrix, and S_m is the ultimate shear strength of the matrix. Thus, equations (5.1) and (5.2) are based on local cell stress levels of the fiber and matrix and on the ultimate strengths of the fiber and matrix. Local fiber and matrix cracking damage, indicating local laminate failure, is assumed to occur when these criteria are exceeded.

When the composite level stresses exceeded his global failure criteria, Chang modelled failure using a different method for both the fiber and composite. For the fiber, Chang degraded fiber properties by reducing the fiber transverse elastic modulus to zero and the fiber longitudinal elastic modulus and shear modulus according to an experimentally determined Weibull distribution. Chang degraded the matrix properties by reducing the matrix transverse elastic modulus to zero. For this work, when the fiber or matrix criteria of equations (5.1) and (5.2) was exceeded, the respective elastic moduli and shear moduli for all directional combinations were reduced by a factor to near zero. Actual reduction to zero was not possible using numerical methods due to resultant singularities in the matrix equations.

C. FEM DAMAGE PROGRESSION STUDY

As noted above, comparison to and extension of the Chang research was a desired goal. Thus, the material chosen for this numerical analysis was based on the Fiberite T300/1034-C graphite epoxy composite which was also used for the Chang work. A cross-ply polymer matrix composite was studied: a $[0/90]_s$ laminate. The fiber and matrix properties were "reverse engineered" from the smeared composite properties presented by Chang. The fiber and matrix properties were determined by an interactive trial and error method utilizing the Kwon cell model. Table 5.1 below shows the Chang smeared properties and the calculated fiber and matrix properties. Fiber volume was calculated to be 50%.

TABLE 5.1 GRAPHITE EPOXY T300/1034-C PROPERTIES

Property	Composite - Chang Smeared	Fiber Calculated	Matrix Calculated
Longitudinal Elastic Modulus (Msi)	21.3	40.0	0.50
Poisson's Ratio	0.30	0.23	0.40
Longitudinal Tensile Strength (Ksi)	251	560	5.0
Shear Strength (Ksi)	19.4	NA	23
Transverse Tensile Strength	9.65	NA	5.0

The FEM program discussed earlier in this report was modified to simulate damage progression. The composite laminate was simulated with a one-eighth model due to symmetry. The one-eighth model laminate plate was 0.5 inches wide, 4.0 inches long, and 0.125 inches thick. Hole radius was one-fourth of the laminate model width at 0.125 inches. Figure 5.1 displays a scaled version of the specimen one-eighth model. A program control loop was implemented to increase the applied end tension up to 72.0 Ksi in increments of either 6.0 Ksi or 7.2 Ksi, depending on the number of load iterations chosen. The tension was applied in the 'x' direction. Within each load increment, a conditional program loop tested for failure; recorded and wrote failure output data; and iterated to re-compute degraded stiffness properties, re-solve for new displacements, and re-calculate to determine cell stresses until the failure criteria indicated no further failures for the current load increment.

For the $[0/90]_s$ composite laminate, total matrix failure occurred in the 90° layer at approximately 36 Ksi. The matrix failure occurred perpendicular to the applied load exactly along the region of maximum stress according to classical theory. Total specimen failure occurred at 54 Ksi when the fiber in the 0° layer failed across the specimen. The fiber failure around the hole in the 0° layer initiated 78.5° to 90° off the axis of the applied load, and then progressed along at 66° to 78.5° off the axis of the applied load. At failure, the fiber failed simultaneously along the outer specimen elements at 66° to 78.5° off the axis of the applied load. These results are displayed in Figures 5.2 through 5.10 on the following pages. Chang modelled a $[(0/90)_6]_s$ laminate for numerical prediction of failure. For this similar laminate with the same width-to-diameter ratio

(W/D=4.0), Chang observed failure at approximately 52 Ksi with the failure path about 75° off the axis of the applied load. Thus, the current results show good agreement with previous research in this area.

The [0/90]_n composite laminate was re-modelled with end displacements applied as compared to above, when end forces which are equivalent to end stress tractions, were applied. Failure load was within 5% of the results above. The failure path was also similar to the results discussed above.

These results differ only slightly from the Chang analytical results. A primary cause for the slight difference probably lies with the "reverse engineered" fiber and matrix properties and fiber volume used for this study. A secondary difference is the failure criteria applied. The failure degradation model used for this current study was somewhat severe, in that properties were reduced to the threshold of numerical singularity. However, the current failure model is desirable from the point of simplicity.

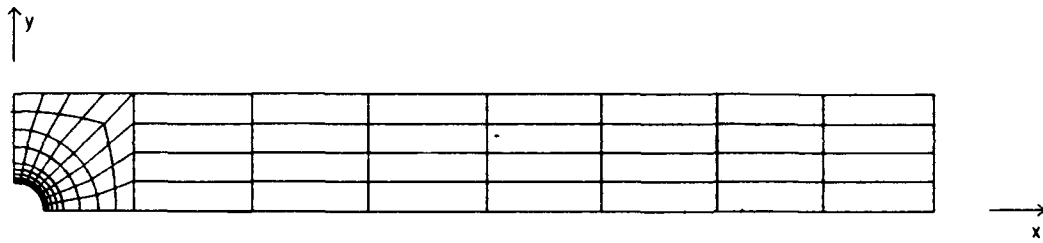


Figure 5.1 - X-Y Plane View Of The FEM One-Eighth Model Of A Composite Plate With A Circular Center Hole.

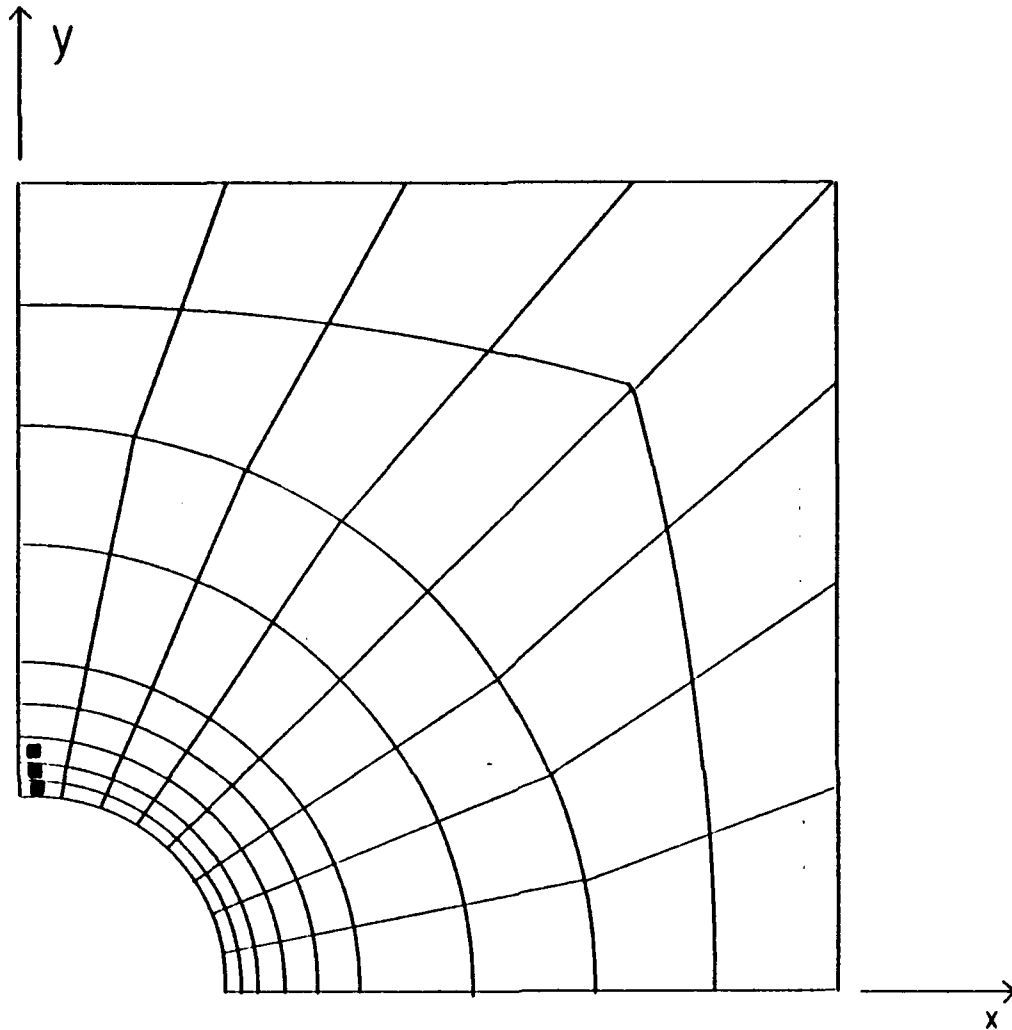


Figure 5.2 - Damage Progress At 12.0 Ksi Applied Stress For [0/90], T300/1034-C Graphite Epoxy Composite Laminate Plate With Center Hole.

Note: The small circles indicate fiber failure. The small boxes indicate matrix failure. Hollow symbols indicate the 0 degree layer. Solid symbols indicate the 90 degree layer.

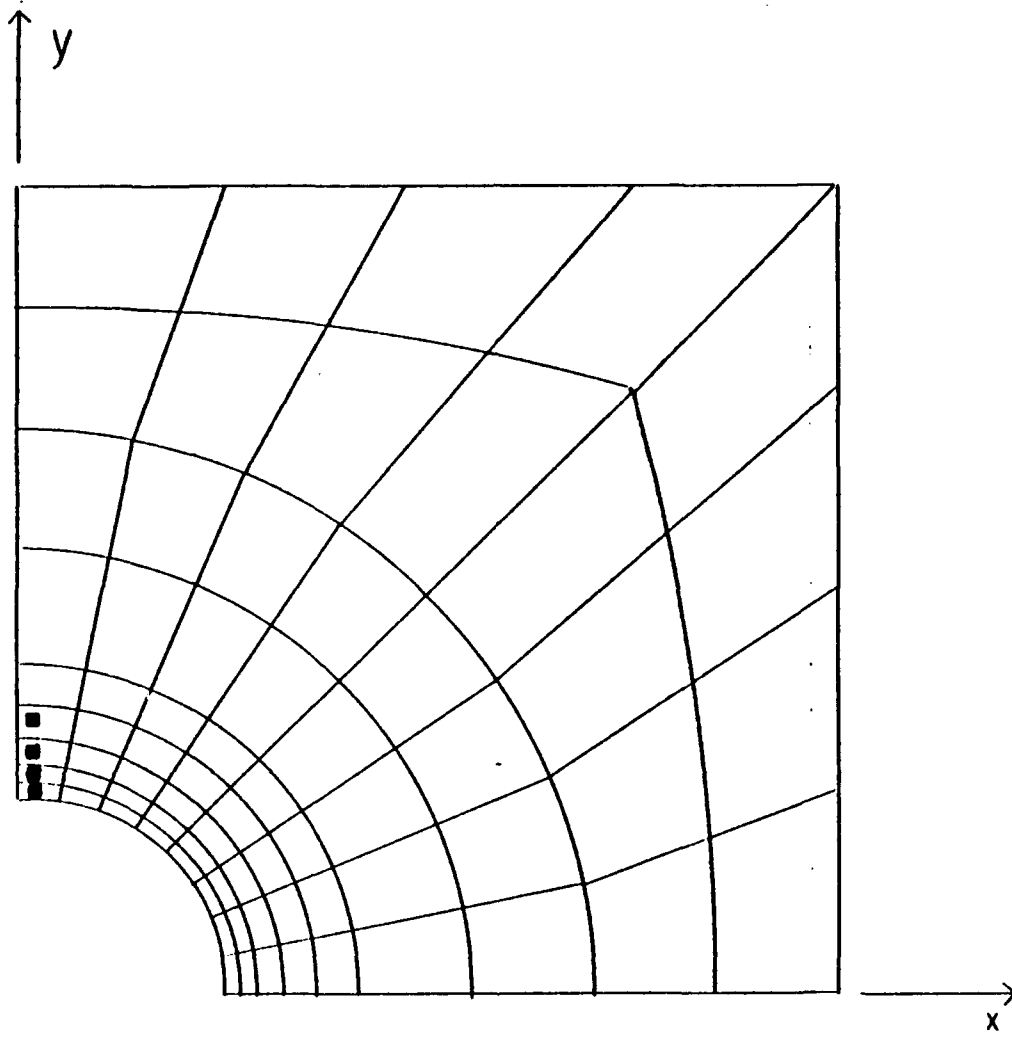


Figure 5.3 - Damage Progress At 18.0 Ksi Applied Stress For [0/90], T300/1034-C Graphite Epoxy Composite Laminate Plate With Center Hole.

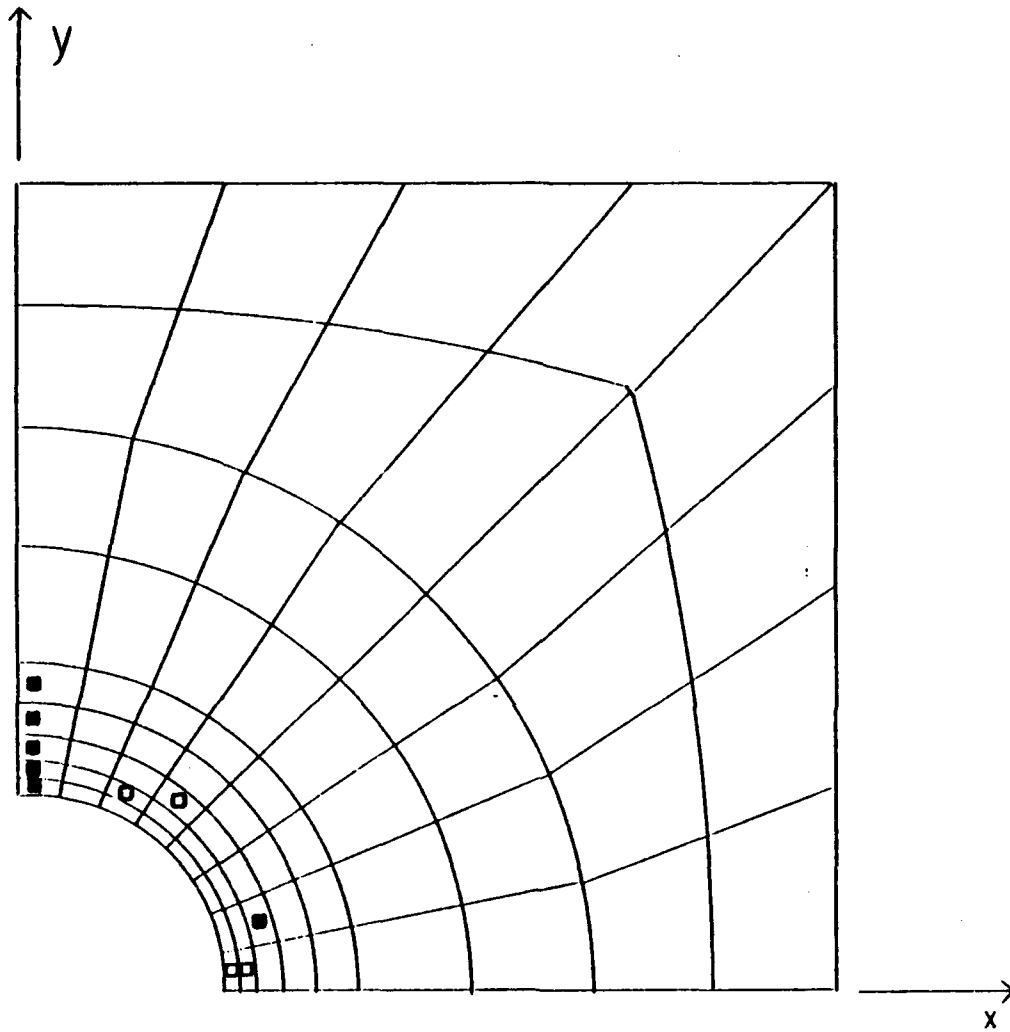


Figure 5.4 - Damage Progress At 24.0 Ksi Applied Stress For [0/90], T300/1034-C Graphite Epoxy Composite Laminate Plate With Center Hole.

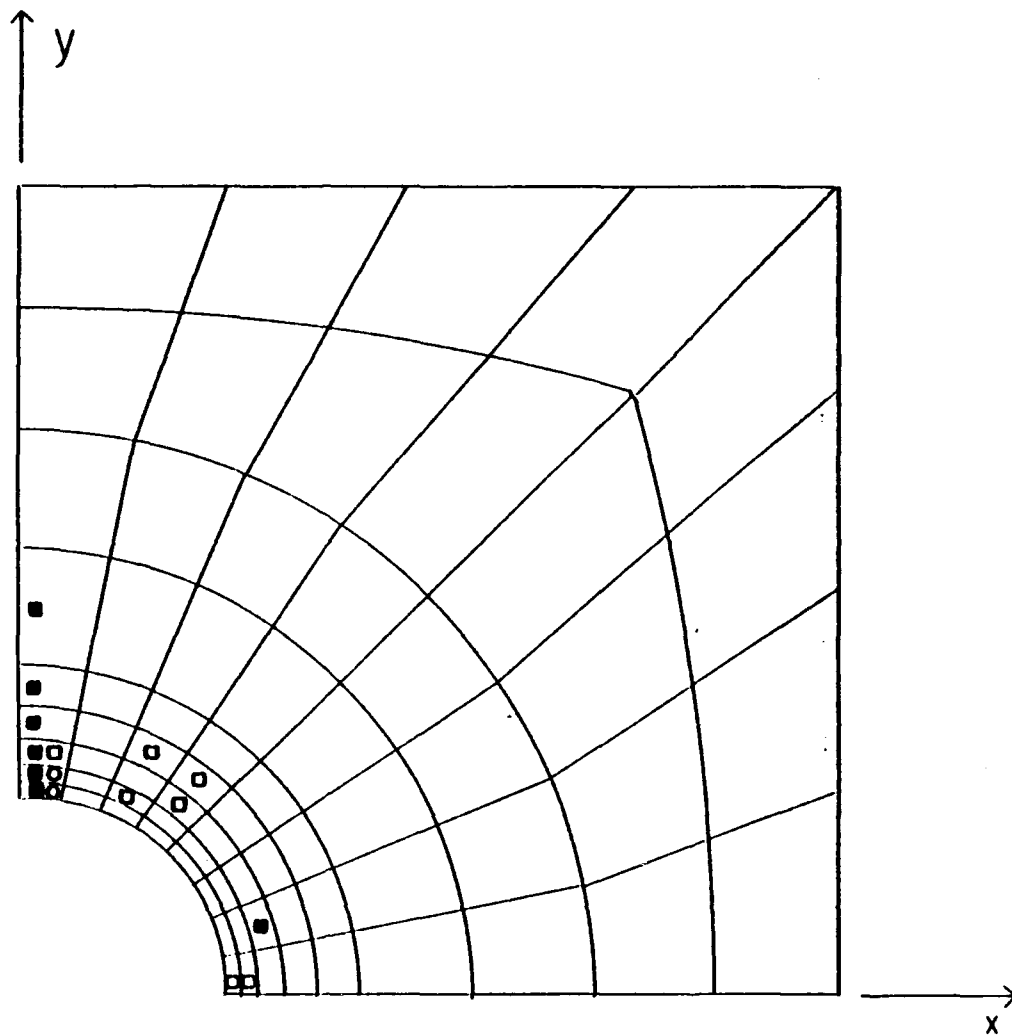


Figure 5.5 - Damage Progress At 30.0 Ksi Applied Stress For [0/90], T300/1034-C Graphite Epoxy Composite Laminate Plate With Center Hole.

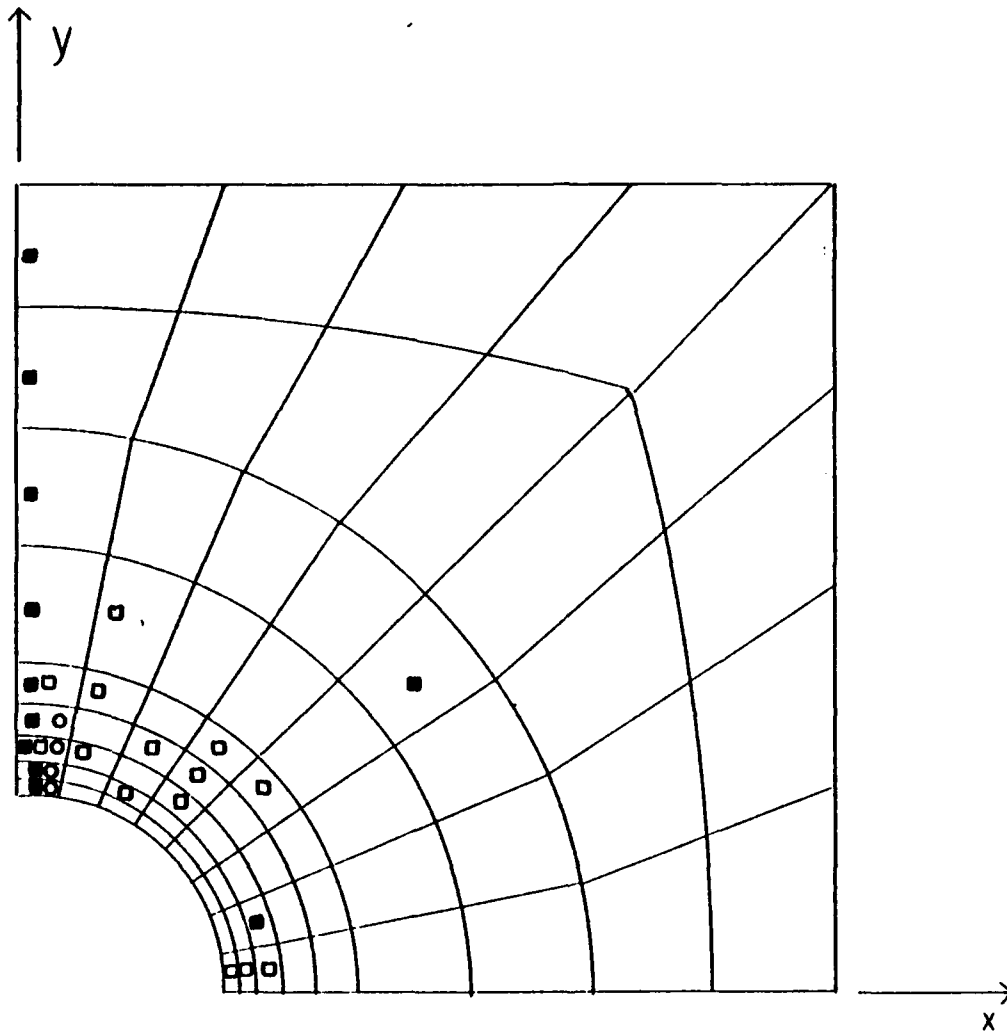


Figure 5.6 - Damage Progress At 36.0 Ksi Applied Stress For [0/90], T300/1034-C Graphite Epoxy Composite Laminate Plate With Center Hole.

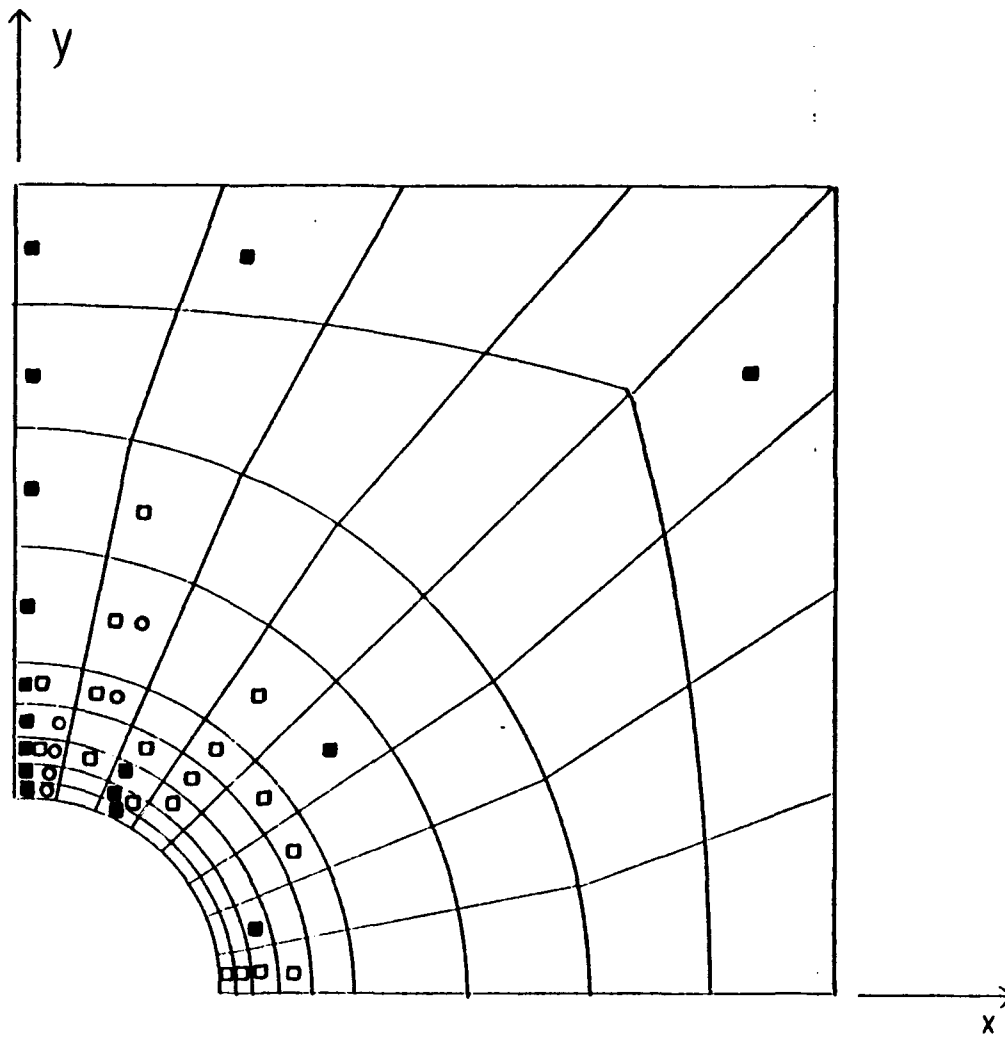


Figure 5.7 - Damage Progress At 42.0 Ksi Applied Stress For [0/90], T300/1034-C Graphite Epoxy Composite Laminate Plate With Center Hole.

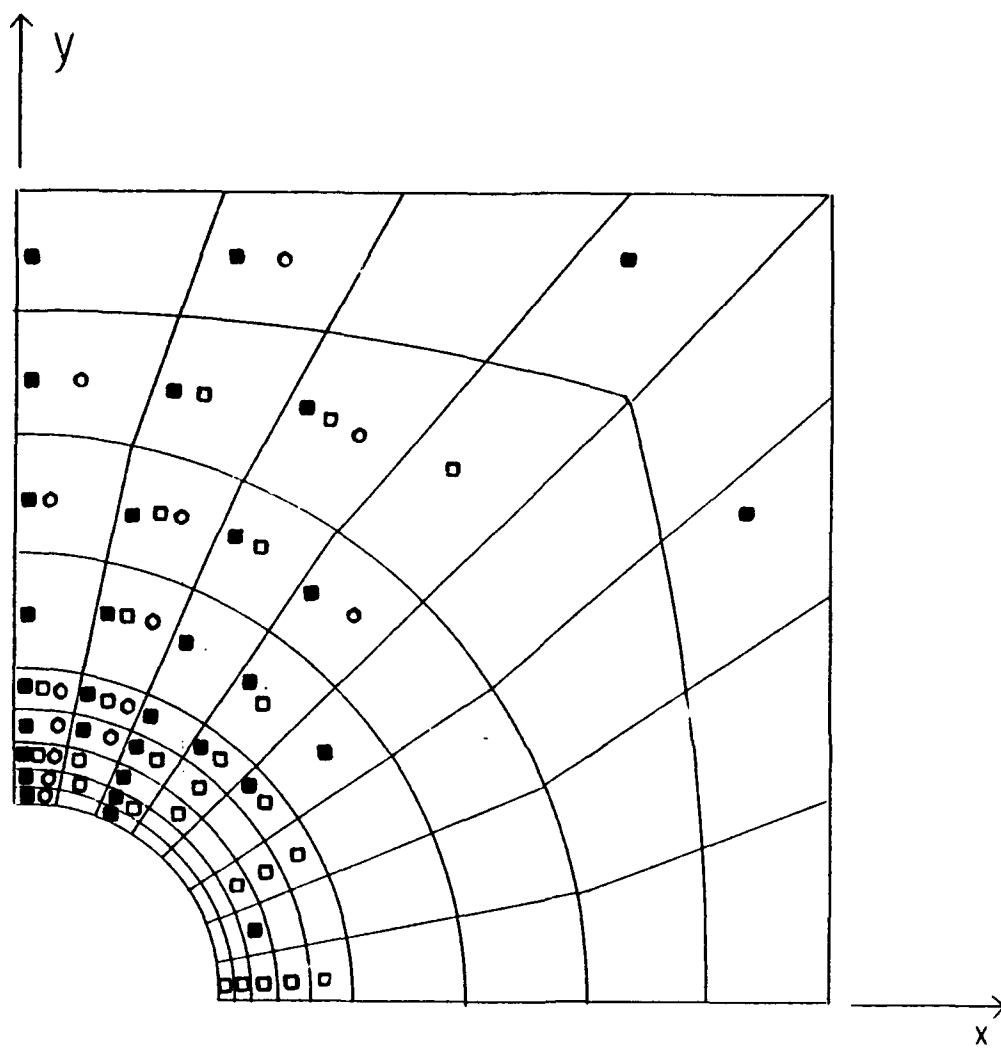


Figure 5.8 - Damage Progress At 48.0 Ksi Applied Stress For [0/90], T300/1034-C Graphite Epoxy Composite Laminate Plate With Center Hole.

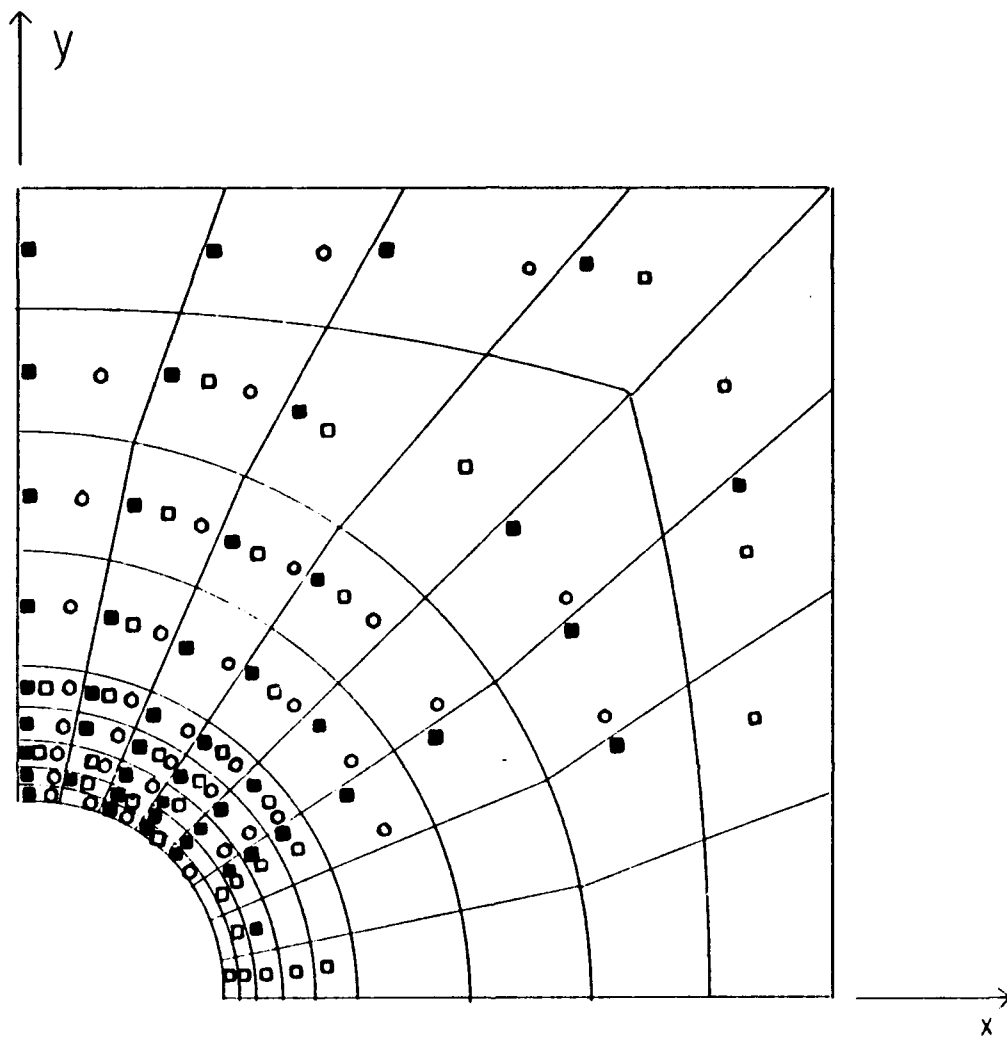


Figure 5.9 - Damage Progress At 54.0 Ksi Applied Stress For [0/90], T300/1034-C Graphite Epoxy Composite Laminate Plate With Center Hole.

VI SUMMARY AND CONCLUSIONS

A. SUMMARY

The new micromechanical model for composite properties developed by Kwon [Ref. 12] was readily incorporated into finite element analysis of composite structural specimens. The Kwon micromechanical model also provided for useful micro-level fiber and matrix stresses in the finite element post-processor subroutines. The fiber and matrix stresses were used to initiate stiffness reduction correlations for material property degradation and failure criteria for damage progression until failure.

The stiffness reduction correlation developed for SiC/CAS ceramic matrix composites was implemented in the finite element analysis based on micro-level matrix stresses determined from the Kwon micromechanical cell model. A stiffness reduction correlation was developed by using finite element analysis of a unidirectional SiC/CAS composite. The stiffness reduction correlation was based on a Weibull type function. Stiffness reduction predictions for the $[0_3/90/0_3]$ SiC/CAS composite showed very good agreement with experimental results of Wang [Ref. 30]. Stiffness reduction predictions for the $[0_3/90_3/0_3]$ SiC/CAS showed good agreement with experimental results.

Thermal residual stresses were incorporated into the stiffness reduction correlation and finite element analysis for three SiC/CAS composite laminates. The unidirectional laminate was used to determine the initial stiffness reduction with thermal residual stress correlation. The finite element analysis predictions for the $[0_3/90/0_3]$ SiC/CAS composite

showed markedly improved agreement with experimental results. However, the revised prediction for stiffness reduction of a $[0_3/90_3/0_3]$ composite showed little discernable improvement in matching experimental results as compared with the stiffness reduction correlation without thermal residuals stress included.

Damage progression and failure studies were performed using finite element analysis with the Kwon micromechanical model for a graphite/epoxy (T300/1034-C) cross-ply composite laminate with a center hole. The finite element analysis for this study predicted the failure load and path with very good correlation to the previous work of Chang [Ref. 38].

B. CONCLUSIONS

The micromechanical cell model developed by Kwon [Ref. 12] can be readily implemented into finite element analysis of composite structures. The initial studies performed in this current work indicate good correlation with experimental work and previous research by other authors. Of course, further analysis of other continuous fiber composite laminate structures with comparison to experimental results is warranted. Also, the micromechanical model need to be modified for discontinuous fiber composites of whisker composites.

The stiffness reduction correlation developed in Chapter III needs further refinement. The predictions for the $[0_3/90_3/0_3]$ cross-ply laminate showed only fair correlation with experimental results. Incorporation of the characteristic damage state or zone concept

based on matrix cracking density into the stiffness reduction weibull function would provide a more clear relationship with the physical mechanism of the matrix cracking.

Including thermal residual stresses in the stiffness reduction correlation generally improved the agreement of the predictions with experimental results. To further improve these predictions, a full three-dimensional thermal residual stress analysis based on the Kwon micromechanical model should be employed. Also, more detailed information on composite fabrication practice with regard to heating and temperature might be useful to improve the computation of thermal residual stress.

The computation of fiber and matrix stress at the micromechanical level is an exceptionally powerful result of the Kwon micromechanical cell method. This method provides an outstanding physical foundation for future study of composite structural stiffness degradation, damage and failure analysis.

LIST OF REFERENCES

1. Agarwal, B.D. and Broutman, L. J., *Analysis And Performance Of Fiber Composites*, John Wiley & Sons, New York, 1990.
2. Chawla, K. K., *Composite Materials*, Springer Verlag, New York, pp. 178-189, 1987.
3. Chamis, C. C., "NASA Tech. Memo. 83320", presented at the 38th Annual Conference of Society of Plastics Industry (SPI), Houston, Texas, February 1983.
4. Chamis, C. C. and Sendekyj, G. P., "Critique on Theories Predicting Thermoelastic Properties of Fibrous Composites," *Journal of Composite Materials*, 2, pp 332-358, 1968.
5. Jones, R. M., *Mechanics of Composite Materials*, Hemisphere Publishing Corporation, New York, pp. 98-122, 1975.
6. Kwon, Y. W., "Calculation of Effective Moduli of Fibrous Composites with Micro-Mechanical Damage," *Composite Structures Vol. 25*, pp. 187-192, 1993.
7. Dvorak, G. J., and Bahei-El-Din, Y. A., "Plasticity Analysis of Fibrous Composite," *Transactions of ASME: Journal of Applied Mechanics*, Vol. 49, pp. 327-335, June 1982.
8. Aboudi, J., *Mechanics of Composite Materials: A Unified Micromechanical Approach*, Elsevier, New York, pp. 35-53, 1991.
9. Pecknold, D. A., "A Framework for 3-D Nonlinear Modeling of Thick-Section Composites," DTRC-SME-90/92, *Ship Materials Engineering Department Research and Development Report*, David Taylor Research Center, 1992.
10. Kwon, Y. W., "Material Nonlinear Analysis of Composite Plate Bending Using New Finite Element Formulation," *Computers & Structures*, Volume 41, No. 5, pp. 1111-1117, 1991.
11. Kwon, Y. W., and Byun, K. Y., "Development of a New Finite Element Formulation for the Elasto-Plastic Analysis of Fiber-Reinforced Composites," *Computers & Structures*, Vol. 35, No. 5, pp. 563-570, 1990.

12. Kwon, Y., "Thermo-Elastoviscoplastic Finite Element Plate Bending Analysis of Composites," *Engineering Computations*, Vol. 9, pp. 595-607, July 1992.
13. Ugural, A. C. and Fenster, S. K., *Advanced Strength and Applied Elasticity*, Elsevier, New York, pp. 7-9, 1987.
14. Easley, J. G., *Mechanics of Elastic Structures*, Prentice Hall, Englewood Cliffs, New Jersey, pp. 3-7, 1989.
15. Wang, C. T., *Applied Elasticity*, McGraw-Hill, New York, pp. 1-7, 1953.
16. Sechler, E. E., *Elasticity in Engineering*, John Wiley & Sons, New York, pp. 30-32, 1952.
17. Bickford, W. B., *A First Course in the Finite Element Method*, Irwin, Boston, Massachusetts, pp. 52-59, pp. 287-307, pp. 484-495, 1990.
18. Chandrupatla, T. R. and Begundu, A. D., *Introduction to Finite Element Methods in Engineering*, Prentice Hall, Englewood Cliffs, New Jersey, pp. 1-9, pp. 14-17, pp. 251-262, 1991.
19. Reddy, J. N., *An Introduction to the Finite Element Method*, 2d Ed., McGraw-Hill, New York, pp. 18-40, pp. 246-258, pp. 579-594, 1993.
20. Rao, S. S., *The Finite Element Method in Engineering*, 2d. Ed., Pergamon Press, New York, pp. 257-283, pp. 355-360, 1989.
21. Akin, J. E., *Application and Implementation of the Finite Element Method*, Academic Press, New York, 1982.
22. Chawla, K. K., *Composite Materials*, Springer Verlag, New York, pp. 137-148, 1987.
23. Aveston, J. and Kelly, A., "Theory of Multiple Fracture of Fibrous Composites," *Journal of Materials Science*, Vol. 8, pp. 352-362, 1973.
24. Hahn, H. T. and Tsai, S. W., "On Behavior of Composite Laminates after Initial Failures," *Journal of Composite Materials*, Vol. 8, pp. 288-305, 1974.
25. Garrett, K. W. and Bailey, J. E., "Multiple Transverse Fracture in 90° Cross-Ply Laminates of a Glass Fibre-Reinforced Polyester," *Journal of Materials Science*, Vol. 12, pp. 157-168, 1977.

26. Parvizi, A. Garrett, K. W., and Bailey, J. E., "Constrained Cracking in Glass Fibre-Reinforced Epoxy Cross-Ply Laminates," *Journal of Materials Science*, Vol. 13, pp 195-201, 1978.
27. Reifsnider, K. L., Henneke, E. G., and Stinchcomb, W. W., "Defect-Property Relationships in Composite Materials," AFML-TR-76-81, Part IV, Air Force Materials Laboratory, June, 1979.
28. Talreja, R., "Transverse Cracking and Stiffness reduction in Composite Laminates," *Journal of Composite Materials*, Vol. 19, pp. 355-375, July, 1985.
29. Talreja, R., *Fatigue of Composite Materials*, Technomic Publishing, Lancaster, PA, pp. 41-123, 1987.
30. Wang, S. W., *Processing and Characterization of Continuous Fiber Reinforced Glass and Glass-Ceramic Matrix Composites*, Ph.D Materials Science, Dissertation, University of Delaware, Delaware, December 1990.
31. Kwon, Y. W. and Berner, J. M., "Analysis of Matrix Damage Evolution in Laminated Composite Plates," in submission, July 1993..
32. Kwon, Y. W. and Berner, J. M., "Numerical Modeling of Stiffness Reduction Due to Transverse Cracking in Unidirectional Composites," *Computational Engineering*, ed. by Kwak, B. M. and Tanaka, M., Elsevier, New York, pp. 3-8, 1993.
33. Sambell, R. A., Briggs, A., Phillips, D. C., and Bowen, D. H., "Carbon Fibre Composites With Ceramic And Glass Matrices," *Journal of Material Science*, Vol. 7, pp. 676-681, 1972.
34. Konisch, H. J. and Whitney, J. M., "Approximate Stresses in an Orthotropic Plate Containing a Circular Hole," *Journal of Composite Materials*, Vol. 9, pp. 157-166, 1975.
35. Chang, F. K., Scott, R. A., and Springer, G. S., "Failure of Composite Laminates Containing Pin Loaded Holes -- Method of Solution," *Journal of Composite Materials*, Vol. 18, pp. 255-278, 1984.
36. Chang, F. K., Scott, R. A., and Springer, G. S., "Design of Composite Laminates Containing Pin Loaded Holes," *Journal of Composite Materials*, Vol. 18, pp. 279-289, 1984.
37. Yamada, S. E. and Sun, C. T., "Analysis of Laminate Strength and Its Distribution," *Journal of Composite Materials*, Vol. 12, pp. 275-284, 1978.

38. Chang, F. K., and Chang, K. Y., G. S., "A Progressive Damage Model for Laminated Composites Containing Stress Concentrations," *Journal of Composite Materials*, Vol. 21, pp. 834-855, 1987.
39. Tsai, S. W. and Hahn, H.T., *Introduction to Composite Materials*, Technomic, 1980.

APPENDIX B - THERMAL STRESS DERIVATION USING KWON CELL METHOD

The following derivation has been developed by Dr. Young W. Kwon. The derivation is provided here for completeness and reference.

The foundation for the Kwon micromechanical cell method is based on the relations given in Equation (B.1).

$$\begin{aligned}\bar{\sigma}_{ij} &= V_f \sigma_{ij}^a + \sqrt{V_f} (1 - \sqrt{V_f}) \sigma_{ij}^b + \sqrt{V_f} (1 - \sqrt{V_f}) \sigma_{ij}^c + (1 - \sqrt{V_f})^2 \sigma_{ij}^d & i,j = 1,3 \\ \bar{\epsilon}_{ij} &= V_f \epsilon_{ij}^a + \sqrt{V_f} (1 - \sqrt{V_f}) \epsilon_{ij}^b + \sqrt{V_f} (1 - \sqrt{V_f}) \epsilon_{ij}^c + (1 - \sqrt{V_f})^2 \epsilon_{ij}^d & i,j = 1,3\end{aligned}\quad (B.1)$$

$$\text{let } \alpha = V_f; \beta = \sqrt{V_f} (1 - \sqrt{V_f}); \gamma = (1 - \sqrt{V_f})^2$$

Based on the unit cell as displayed in Figure 1.1, the compatibility equations for stress and strain are given in Equations (B.2) and (B.3).

$$\begin{aligned}\sigma_{22}^a &= \sigma_{22}^b, & \sigma_{22}^c &= \sigma_{22}^d, & \sigma_{33}^a &= \sigma_{33}^c, & \sigma_{33}^b &= \sigma_{33}^d \\ \sigma_{12}^a &= \sigma_{12}^b, & \sigma_{12}^c &= \sigma_{12}^d, & \sigma_{13}^a &= \sigma_{13}^c, & \sigma_{13}^b &= \sigma_{13}^d \\ \sigma_{23}^a &= \sigma_{23}^b, & \sigma_{23}^c &= \sigma_{23}^d, & \sigma_{23}^a &= \sigma_{23}^d\end{aligned}\quad (B.2)$$

$$\begin{aligned}\epsilon_{11}^a &= \epsilon_{11}^b, & \epsilon_{11}^c &= \epsilon_{11}^d, & \epsilon_{11}^a &= \epsilon_{11}^d \\ \epsilon_{22}^a + \epsilon_{22}^b &= \epsilon_{22}^c + \epsilon_{22}^d, & \epsilon_{33}^a + \epsilon_{33}^c &= \epsilon_{33}^b + \epsilon_{33}^d \\ \epsilon_{12}^a + \epsilon_{12}^b &= \epsilon_{12}^c + \epsilon_{12}^d, & \epsilon_{13}^a + \epsilon_{13}^c &= \epsilon_{13}^b + \epsilon_{13}^d\end{aligned}\quad (B.3)$$

The total strain is equal to the sum of the mechanical strain and the thermal strain as given by Equation (B.4).

$$\epsilon_{ij}^{\alpha} = (\epsilon_{\text{mech}})_{ij}^{\alpha} + (\epsilon_{\text{thermal}})_{ij}^{\alpha} \quad (\text{B.4})$$

The generalized Hooke's law relates the mechanical stress to the mechanical strain. From Equation (B.4), the mechanical strain can be composed of the difference of the total strain and the thermal strain. Equation (B.5) shows this result.

$$\sigma_{ij}^{\alpha} = E_{ijkl}^{\alpha} (\epsilon_{\text{mech}})_{ij}^{\alpha} = E_{ijkl}^{\alpha} [\epsilon_{ij}^{\alpha} - (\epsilon_{\text{thermal}})_{ij}^{\alpha}] = E_{ijkl}^{\alpha} \epsilon_{ij}^{\alpha} - E_{ijkl}^{\alpha} (\epsilon_{\text{thermal}})_{ij}^{\alpha} \quad (\text{B.5})$$

An inverse relationship for the mechanical stress can also be developed as shown in the algebraic derivation in Equation (B.6) for an orthotropic material.

$$\begin{aligned}\epsilon_{11} &= C_{11}\sigma_{11} + C_{12}\sigma_{22} + C_{13}\sigma_{33} + \alpha_{11}\Delta T \\ \epsilon_{22} &= C_{21}\sigma_{11} + C_{22}\sigma_{22} + C_{23}\sigma_{33} + \alpha_{22}\Delta T \\ \epsilon_{33} &= C_{31}\sigma_{11} + C_{32}\sigma_{22} + C_{33}\sigma_{33} + \alpha_{33}\Delta T\end{aligned}$$

$$\begin{Bmatrix} \epsilon_{11} - \alpha_{11}\Delta T \\ \epsilon_{22} - \alpha_{22}\Delta T \\ \epsilon_{33} - \alpha_{33}\Delta T \end{Bmatrix} = [C] \begin{Bmatrix} \sigma_{11} \\ \sigma_{22} \\ \sigma_{33} \end{Bmatrix}$$

$$\begin{Bmatrix} \sigma_{11} \\ \sigma_{22} \\ \sigma_{33} \end{Bmatrix} = [C]^{-1} \begin{Bmatrix} \epsilon_{11} - \alpha_{11}\Delta T \\ \epsilon_{22} - \alpha_{22}\Delta T \\ \epsilon_{33} - \alpha_{33}\Delta T \end{Bmatrix} = [E] \left(\begin{Bmatrix} \epsilon_{11} \\ \epsilon_{22} \\ \epsilon_{33} \end{Bmatrix} - \begin{Bmatrix} \alpha_{11}\Delta T \\ \alpha_{22}\Delta T \\ \alpha_{33}\Delta T \end{Bmatrix} \right) \quad (\text{B.6})$$

$$\begin{Bmatrix} \sigma_{11} \\ \sigma_{22} \\ \sigma_{33} \end{Bmatrix} = [E] \begin{Bmatrix} \epsilon_{11} \\ \epsilon_{22} \\ \epsilon_{33} \end{Bmatrix} - [E] \begin{Bmatrix} \alpha_{11}\Delta T \\ \alpha_{22}\Delta T \\ \alpha_{33}\Delta T \end{Bmatrix} = [E] \begin{Bmatrix} \epsilon_{11} \\ \epsilon_{22} \\ \epsilon_{33} \end{Bmatrix} - \begin{Bmatrix} (\sigma_{\text{thermal}})_{11} \\ (\sigma_{\text{thermal}})_{22} \\ (\sigma_{\text{thermal}})_{33} \end{Bmatrix}$$

$$\begin{aligned}\sigma_{11} &= E_{11}\epsilon_{11} + E_{12}\epsilon_{22} + E_{13}\epsilon_{33} + (\sigma_{\text{thermal}})_{11} \\ \sigma_{22} &= E_{21}\epsilon_{11} + E_{22}\epsilon_{22} + E_{23}\epsilon_{33} + (\sigma_{\text{thermal}})_{22} \\ \sigma_{33} &= E_{31}\epsilon_{11} + E_{32}\epsilon_{22} + E_{33}\epsilon_{33} + (\sigma_{\text{thermal}})_{33}\end{aligned}$$

Use shortened format: $(\sigma_t)_{11} = (\sigma_{\text{thermal}})_{11}$, etc.

Equation (B.7) re-writes the stress compatibility equations in terms of mechanical strain and thermal stress that were developed in equation (B.6).

1. $\sigma_{22}^a = \sigma_{22}^b$
 $E_{21}^a \epsilon_{11}^a + E_{22}^a \epsilon_{22}^a + E_{23}^a \epsilon_{33}^a - (\sigma_t)_{22}^a = E_{21}^b \epsilon_{11}^b + E_{22}^b \epsilon_{22}^b + E_{23}^b \epsilon_{33}^b - (\sigma_t)_{22}^b$
2. $\sigma_{22}^c = \sigma_{22}^d$
 $E_{21}^c \epsilon_{11}^c + E_{22}^c \epsilon_{22}^c + E_{23}^c \epsilon_{33}^c - (\sigma_t)_{22}^c = E_{21}^d \epsilon_{11}^d + E_{22}^d \epsilon_{22}^d + E_{23}^d \epsilon_{33}^d - (\sigma_t)_{22}^d$
3. $\sigma_{33}^a = \sigma_{33}^c$
 $E_{31}^a \epsilon_{11}^a + E_{32}^a \epsilon_{22}^a + E_{33}^a \epsilon_{33}^a - (\sigma_t)_{33}^a = E_{31}^c \epsilon_{11}^c + E_{32}^c \epsilon_{22}^c + E_{33}^c \epsilon_{33}^c - (\sigma_t)_{33}^c$
4. $\sigma_{33}^b = \sigma_{33}^d$
 $E_{31}^b \epsilon_{11}^b + E_{32}^b \epsilon_{22}^b + E_{33}^b \epsilon_{33}^b - (\sigma_t)_{33}^b = E_{31}^d \epsilon_{11}^d + E_{32}^d \epsilon_{22}^d + E_{33}^d \epsilon_{33}^d - (\sigma_t)_{33}^d$

(B.7)

Equation (B.8) re-writes the strain compatibility equations in a similar manner.

1. $\epsilon_{11}^a = \epsilon_{11}^b = \epsilon_{11}^c = \epsilon_{11}^d = \bar{\epsilon}_{11}$
2. $\epsilon_{11}^a = \epsilon_{11}^b$
 $(\epsilon_m)_{11}^a + (\epsilon_t)_{11}^a = (\epsilon_m)_{11}^b + (\epsilon_t)_{11}^b$
3. $\epsilon_{11}^a = \epsilon_{11}^c$
 $(\epsilon_m)_{11}^a + (\epsilon_t)_{11}^a = (\epsilon_m)_{11}^c + (\epsilon_t)_{11}^c$
4. $\epsilon_{11}^a = \epsilon_{11}^d$
 $(\epsilon_m)_{11}^a + (\epsilon_t)_{11}^a = (\epsilon_m)_{11}^d + (\epsilon_t)_{11}^d$
5. $\epsilon_{22}^a + \epsilon_{22}^b = \epsilon_{22}^c + \epsilon_{22}^d$
 $(\epsilon_m)_{22}^a + (\epsilon_t)_{22}^a + (\epsilon_m)_{22}^b + (\epsilon_t)_{22}^b = (\epsilon_m)_{22}^c + (\epsilon_t)_{22}^c + (\epsilon_m)_{22}^d + (\epsilon_t)_{22}^d$
6. $\epsilon_{33}^a + \epsilon_{33}^c = \epsilon_{33}^b + \epsilon_{33}^d$
 $(\epsilon_m)_{33}^a + (\epsilon_t)_{33}^a + (\epsilon_m)_{33}^c + (\epsilon_t)_{33}^c = (\epsilon_m)_{33}^b + (\epsilon_t)_{33}^b + (\epsilon_m)_{33}^d + (\epsilon_t)_{33}^d$

(B.8)

Combining terms from Equations (B.1), (B.7), and (B.8) yields a system of equations where the mechanical cell strains can be expressed in terms of the composite average strains as shown in Equation (B.9).

$$\begin{aligned}
 \epsilon_{22}^a + \epsilon_{22}^b - \epsilon_{22}^c - \epsilon_{22}^d &= 0 \\
 \epsilon_{33}^a - \epsilon_{33}^b + \epsilon_{33}^c - \epsilon_{33}^d &= 0 \\
 \alpha \epsilon_{22}^a + \beta \epsilon_{22}^b + \beta \epsilon_{22}^c + \gamma \epsilon_{22}^d &= \bar{\epsilon}_{22} \\
 \alpha \epsilon_{33}^a + \beta \epsilon_{33}^b + \beta \epsilon_{33}^c + \gamma \epsilon_{33}^d &= \bar{\epsilon}_{33} \\
 E_{22}^a \epsilon_{22}^a - E_{22}^b \epsilon_{22}^b + E_{23}^a \epsilon_{33}^a - E_{23}^b \epsilon_{33}^b &= (E_{21}^b - E_{21}^a) \bar{\epsilon}_{11} + (\sigma_{11})^a - (\sigma_{11})^b \\
 E_{32}^a \epsilon_{22}^a - E_{32}^c \epsilon_{22}^c + E_{33}^a \epsilon_{33}^a - E_{33}^c \epsilon_{33}^c &= (E_{31}^c - E_{31}^a) \bar{\epsilon}_{11} + (\sigma_{11})^a - (\sigma_{11})^c \\
 E_{22}^c \epsilon_{22}^c - E_{22}^d \epsilon_{22}^d + E_{23}^c \epsilon_{33}^c - E_{23}^d \epsilon_{33}^d &= (E_{21}^d - E_{21}^c) \bar{\epsilon}_{11} + (\sigma_{11})^c - (\sigma_{11})^d \\
 E_{32}^b \epsilon_{22}^b - E_{32}^d \epsilon_{22}^d + E_{33}^b \epsilon_{33}^b - E_{33}^d \epsilon_{33}^d &= (E_{31}^d - E_{31}^b) \bar{\epsilon}_{11} + (\sigma_{11})^b - (\sigma_{11})^d
 \end{aligned} \tag{B.9}$$

Equation (B.9) can be written in matrix/vector equation format as in Equation (B.10).

$$\left\{ \epsilon_{ij}^a \right\} \left[A \right] = \left\{ f(\bar{\epsilon}_{ij}) \right\} \tag{B.10}$$

Displacement based FEM programs will solve for composite macro-level displacements. Postprocessing modules first convert these displacement values into composite strains. Inverting Equation (B.10) allows solving for the micro-level cell strains. In summary, the solution procedure for thermal stresses becomes:

1. Compute the smeared property matrix [D] and the thermal stress vector $\{\sigma_t\}$.
2. Compute the displacement vector $\{d\}$ from $[K]\{d\}=\{F\}$, where vector $\{F\}$ includes both mechanical and thermal loads.
3. Compute the composite strain vector $\{\epsilon\}$.
4. Compute the fiber and matrix cell strains $\{\epsilon^a\}$.
5. Compute the fiber and matrix mechanical strains $\{\epsilon_m^a\}$ from the equation $\{\epsilon_m^a\} + \{\epsilon_t^a\} = \{\epsilon^a\}$.
6. Compute the fiber and matrix cell stresses $\{\sigma^a\}$ from $\{\sigma^a\} = [E] \{\epsilon_m^a\}$.
7. Compute the composite stress $\{\sigma\}$ from $\{\sigma^a\}$.

INITIAL DISTRIBUTION LIST

1. Defense Technical Information Center 2
Cameron Station
Alexandria, Virginia 22304-6145
2. Library, Code 52 2
Naval Postgraduate School
Monterey, California 93943-5000
3. Department Chairman, Code ME 1
Department of Mechanical Engineering
Naval Postgraduate School
Monterey, California 93943-5000
4. Professor Young W. Kwon, Code ME/Kw 2
Department of Mechanical Engineering
Naval Postgraduate School
Monterey, California 93943-5000
5. Joseph M. Berner 1
3920 Dillingersville Road
Zionsville, Pennsylvania 18092
6. Dr. Shaio-Wen Wang 1
Advanced metallic & Ceramic Branch (6063)
Aircraft Division
Naval Air Warfare Center
Warminster, PA 18974-0591
7. Dr. Vincent J. Castelli 1
Senior Research Scientist
Naval Surface Warfare Center
3A Leggett Circle
Composites and Resins Branch, Code 644
Annapolis, MD 21402-5067

8. **Mr. David Bonnani** 1
Naval Surface Warfare Center, Carderock Div.
Code 1720.2
Bethesda, Maryland 20084-5000

9. **Dr. Y. D. Rajapakse** 1
Office of Naval Research
Mechanics Division, Code 1132
800 North Quincy Street
Arlington, Virginia 22217-5000

10. **Dr. Phillip B. Abraham** 1
Office of Naval Research
Mechanics Division, Code 1132
Arlington, Virginia 22217-5000

11. **Dr. Roshdy S. Barsoum** 1
Director of Solid Mechanics Program
Office of Naval Research
800 North Quincy Street
Arlington, VA 22217-5000